# ICES REPORT 17-33

**November 2017**

# Blended B-Spline Construction on Unstructured Quadrilateral and Hexahedral Meshes with Optimal Convergence Rates in Isogeometric Analysis

**by**

Xiaodong Wei, Yongjie Jessica Zhang, Deepesh Toshniwal, Hendrik Speleers, Xin Li, Carla Manni,John A. Evans, and Thomas J.R. Hughes


**The Institute for Computational Engineering and Sciences**
The University of Texas at Austin
Austin, Texas 78712

*Reference: Xiaodong Wei, Yongjie Jessica Zhang, Deepesh Toshniwal, Hendrik Speleers, Xin Li, Carla Manni,John A. Evans, and Thomas J.R. Hughes, "Blended B-Spline Construction on Unstructured Quadrilateral and Hexahedral Meshes with Optimal Convergence Rates in Isogeometric Analysis," ICES REPORT 17-33, The Institute for Computational Engineering and Sciences, The University of Texas at Austin, November 2017.*

# Blended B-Spline Construction on Unstructured Quadrilateral and Hexahedral Meshes with Optimal Convergence Rates in Isogeometric Analysis

Xiaodong Wei[a], Yongjie Jessica Zhang[a,*], Deepesh Toshniwal[b], Hendrik Speleers[c], Xin Li[d], Carla Manni[c], John A. Evans[e], Thomas J.R. Hughes[b]

[a]*Department of Mechanical Engineering, Carnegie Mellon University, Pittsburgh, PA 15213, USA*
[b]*Institute for Computational Engineering and Sciences, The University of Texas at Austin, Austin, TX 78712, USA*
[c]*Department of Mathematics, University of Rome "Tor Vergata", Italy*
[d]*School of Mathematical Sciences, University of Science and Technology of China, Hefei, Anhui, China*
[e]*Department of Aerospace Engineering Sciences, University of Colorado Boulder, Boulder, CO 80309, USA*

**Abstract**

We present a novel blended B-spline method to construct bicubic/tricubic splines over unstructured quadrilateral and hexahedral meshes for isogeometric analysis. $C^1$ and (truncated) $C^2$ B-spline functions are used in regular elements, whereas $C^0$ and (truncated) $C^1$ B-spline functions are adopted in boundary elements and interior irregular elements around extraordinary edges/vertices. The truncation mechanism is employed for a seamless transition from irregular to regular elements. The resulting regularity of the blended construction is $C^2$-continuous everywhere except $C^0$-continuous around extraordinary edges and $C^1$-continuous across the interface between irregular and regular elements. The blended B-spline construction yields consistent parameterization during refinement and exhibits optimal convergence rates. Spline functions in the blended construction form a non-negative partition of unity, are linearly independent, and support Bézier extraction such that the construction can be used in existing finite element frameworks. Several examples provide numerical evidence of optimal convergence rates.

*Keywords:* Blended B-Spline Construction, Extraordinary Vertices/Edges, Optimal Convergence Rates, Unstructured Quadrilateral and Hexahedral Meshes, Isogeometric Analysis.

## 1. Introduction

Isogeometric analysis (IGA) was introduced to bridge the gap between computer-aided design (CAD) and traditional finite element analysis (FEA) by utilizing the same basis of a CAD representation in analysis [13, 8]. In addition to CAD representations, unstructured quadrilateral (quad) and hexahedral (hex) meshes can also serve as important input control meshes[1] for IGA. For instance, many techniques have been developed to convert imaging data to such meshes [36]. Unstructured quad/hex meshes inevitably involve extraordinary vertices/edges. In the interior of a quad/hex mesh, an *extraordinary vertex/edge* is a vertex/edge shared by other than four quad/hex elements, respectively. Endpoints of extraordinary edges in 3D are also extraordinary vertices. Generally, in a hex mesh, there exist 3D extraordinary vertices that cannot be obtained by sweeping 2D counterparts. How to deal with extraordinary vertices/edges is the key to employing unstructured quad/hex meshes in IGA, and developing a spline basis with desired properties, such as non-negative partition of unity, linear independence, smoothness (preferably $G^1$ or better), nested

*Corresponding author: Yongjie Jessica Zhang. Tel: (412) 268-5332; Fax: (412) 268-3348; Email: *jessicaz@andrew.cmu.edu*.

[1]The term "control mesh" implies the odd degree case, where each control point corresponds to a mesh vertex.

spline spaces, and exhibiting optimal convergence rates, is a challenge. We are particularly interested in optimal convergence rates in this paper.

While advances have been made for unstructured quad meshes, very few methods [5, 29, 31] have been studied for unstructured hex meshes in IGA, and none exhibits optimal convergence rates while maintaining higher-order smoothness. Catmull-Clark subdivision [5, 16, 32, 33] has often been used for unstructured quad/hex meshes, where a patch near an extraordinary vertex is represented by an infinite series of sub-patches of uniform bicubic/tricubic B-splines. Such an infinite representation needs an enormous number of Gauss points in analysis to guarantee integration accuracy [16, 21, 32, 33]. However, optimal convergence has not been observed even with accurate integration [16]. Manifold splines were used in IGA and optimal convergence rates were observed [15], but this method also requires many integration points. A template-based $C^0$-parameterization method, taking advantage of T-spline local knot vectors, was proposed to convert unstructured quad meshes to watertight T-spline representations [30, 29]. However, this method was focused on geometry and convergence behavior was not studied. The multi-patch B-spline/NURBS methods, including $C^0$-parameterization [24, 4] and $G^1$-parameterization methods [14, 7], treat the region around an extraordinary vertex in a multi-patch manner. Although optimal convergence rates can be achieved in both $C^0$ and $G^1$ constructions, locally splitting an unstructured mesh (especially an unstructured hex mesh) around extraordinary vertices/edges into multiple B-spline/NURBS patches is not trivial, primarily because many extraordinary vertices might be in close proximity. Global refinement can separate such adjacent extraordinary vertices, but it introduces a large number of unnecessary degrees of freedom (DOF). Bézier extraction expresses basis functions around extraordinary vertices as linear combinations of Bernstein polynomials [23, 34, 17, 31, 35, 27, 26]. In [35], a dynamic weighted refinement scheme was proposed to improve the convergence rate, but optimal optimal convergence rates were still not achieved. With a $C^1$-continuous construction in the vicinity of extraordinary points in 2D, two methods were proposed based on degenerated bivariate Bézier patches [20]: one in the context of PHT-splines [10] with emphasis on refinability around extraordinary vertices [17], and the other from the isogeometric analysis point of view [27]. Both methods have achieved optimal convergence rates.

It is straightforward to construct global $C^0$ parameterization using Bézier basis functions, which, however, is not favored as it engenders too many DOF, especially in 3D. We are interested in building a subspace that yields optimal convergence rates, but with substantially fewer DOF. The challenging problem here is how to construct consistent $C^0$ parameterization for irregular elements that can be seamlessly connected with regular $C^2$ parameterization. A *consistent parameterization* maps a given point in the parametric domain to the same point in the physical domain before and after refinement. Extra DOF need to be added in irregular elements to maintain consistent parameterization, but the number needs to be minimized. In this paper, we present a novel blended $C^0/C^1/C^2$ B-spline parameterization method, referred to as the $C012$ construction, on unstructured quad and hex meshes that can achieve optimal convergence rates with minimal extra DOF introduced. Taking an unstructured quad/hex mesh as the input control mesh, we distinguish two submeshes: an *irregular submesh* composed of boundary elements as well as irregular elements that contain extraordinary vertices, and a *regular submesh* consisting of regular elements only. We use bicubic/tricubic splines throughout this paper. $C^0$ and (truncated) $C^1$ B-spline functions are added in the irregular submesh, whereas $C^1$ and (truncated) $C^2$ B-spline functions are adopted in the regular submesh. Across the interface of the two submeshes, the truncation mechanism [12] is used to connect them. The resulting geometry of a blended B-spline representation is $C^2$-continuous in the regular subdomain, $C^1$-continuous across the two subdomains, and $C^0$-continuous in the irregular subdomain. Such a blended construction limits the influence of extraordinary vertices/edges to within their one-ring neighborhoods. Necessary DOF (i.e., Bézier control points) are introduced in the irregular submesh to guarantee consistent parameterization. The refinement scheme of the blended construction is simply the knot insertion algorithm [1, 19]. The basis functions in the blended construction form a non-negative partition of unity, are globally linearly independent, and support Bézier extraction. Optimal convergence rates are observed for this construction in all tested examples with unstructured quad/hex meshes.

The remainder of the paper is organized as follows. A review of B-splines and Bézier extraction on unstructured quad and hex meshes is given in Section 2. We then discuss the blended B-spline construction on unstructured quad and hex meshes in Sections 3 and 4, respectively. Several properties of the blended

B-spline construction are proved in Section 5. We present in Section 6 numerical examples to verify that the proposed method can achieve optimal convergence rates. Conclusions and future work are presented in Section 7. Two variants of the $C012$ construction are given in Appendix A.

## 2. Review of B-Splines and Bézier Extraction on Unstructured Quad/Hex Meshes

In this section, we review B-splines and Bézier extraction on unstructured quad/hex meshes. Related details can be found in [19, 8, 22, 31].

### *2.1. B-Splines*

We start with a brief review to B-splines. A univariate B-spline is defined on a set of non-decreasing real numbers, the so-called *knot vector* denoted by $\Xi = \{\xi_1, \xi_2, \ldots, \xi_{n+p+1}\}$, where $\xi_i$ is the $i$-th knot, $n$ is the number of B-spline basis functions and $p$ is the polynomial degree. $[\xi_i, \xi_{i+1}]$ $(1 \leq i \leq n+p)$ is called the *knot interval*. A knot vector is *uniform* if all the knot intervals have the same length. B-spline basis functions $\{N_{i,p}\}_{i=1}^{n}$ can be obtained by the Cox-de Boor recursion formula [9], starting from $p = 0$,

$$N_{i,0}(\xi) = \begin{cases} 1 & \text{if } \xi_i \leq \xi < \xi_{i+1} \\ 0 & \text{otherwise} \end{cases} \tag{1}$$

and for $p \geq 1$, we have

$$N_{i,p}(\xi) = \frac{\xi - \xi_i}{\xi_{i+p} - \xi_i} N_{i,p-1}(\xi) + \frac{\xi_{i+p+1} - \xi}{\xi_{i+p+1} - \xi_{i+1}} N_{i+1,p-1}(\xi). \tag{2}$$

A B-spline basis function $N_{i,p}$ is non-negative and has a local support in $[\xi_i, \xi_{i+p+1}]$. $N_{i,p}$ is $C^\infty$-continuous inside knot spans $(\xi_{i+k}, \xi_{i+k+1})$ and $C^{p-m}$-continuous across knots with multiplicity $m$ $(m \leq p+1)$. Bivariate and trivariate B-spline basis functions are simply tensor products of univariate ones.

In Fig. 1, we show several cubic $C^2$ and $C^1$ B-spline basis functions. Later we will use them in our blended B-spline construction. For instance in Fig. 1(a), given a uniform knot vector of degree three, $\{0, 1, \ldots, 7\}$, there are four $C^2$ B-spline basis functions. With another knot vector also of degree three in Fig. 1(c), $\{0, 0, 1, 1, \ldots, 7, 7\}$, where every knot is repeated, twelve $C^1$ B-spline functions are defined. The corresponding $C^2$ and $C^1$ functions with support on the knot span $[3, 4]$ are shown in Fig. 1(b, d), respectively. We will only consider bi- and tri-cubic splines, so in the rest of the paper $p = 3$ in each parametric direction.

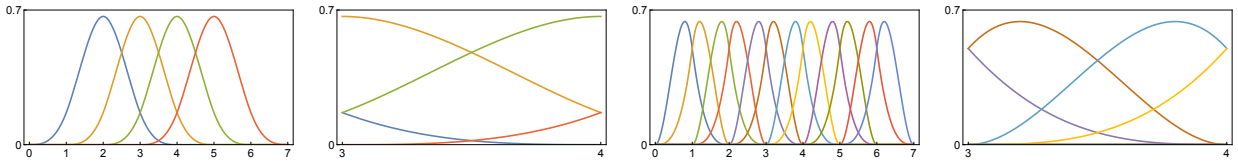


(a) (b) (c) (d)

Figure 1: $C^2$ and $C^1$ B-spline functions in 1D. (a) $C^2$ B-spline functions defined on a uniform knot vector, (b) the $C^2$ functions with support on the knot interval $[3, 4]$, (c) $C^1$ B-spline functions defined on a knot vector with each knot repeated, and (d) the $C^1$ B-spline functions with support on the knot interval $[3, 4]$.

### *2.2. Bézier Extraction on Unstructured Quad Meshes*

With reference to Fig. 2, we introduce several terminologies to facilitate our developments. An unstructured quad mesh, which can be treated as a T-mesh without T-junctions [25], consists of vertices (or control points), edges and quad faces (or elements). The number of elements sharing a vertex is called its *valence*. An interior vertex of valence other than four, as well as a boundary vertex of valence other than two or one, is called an *extraordinary vertex*. Edges touching an extraordinary vertex are called *spoke edges*. An

element is a boundary element if it has at least one vertex lying on the boundary, and otherwise it is an interior element. An interior element is an *irregular element* if any of its four vertices is an extraordinary vertex. Otherwise it is a regular element. Note that a boundary element may also have certain vertices being extraordinary vertices, but in this paper we do not further distinguish such cases, and instead we treat all the boundary elements as irregular elements to simplify the implementation. An element and its one-ring neighboring elements (i.e., elements sharing vertices with it) form a *local (control) mesh* of the element. Bézier extraction for an element involves its local mesh. Each edge is assigned with a knot interval, which is used to define coefficients in Bézier extraction and will be explained in detail as follows. Uniform knot vectors are assumed in unstructured meshes to satisfy the condition that knot intervals of opposite edges in each element coincide [25], which also simplifies Bézier extraction for irregular elements.

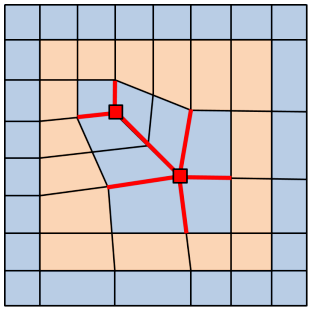

Figure 2: An unstructured quad mesh with two extraordinary vertices (red squares). Spoke edges are marked in red. Irregular and regular elements are shaded blue and orange, respectively.

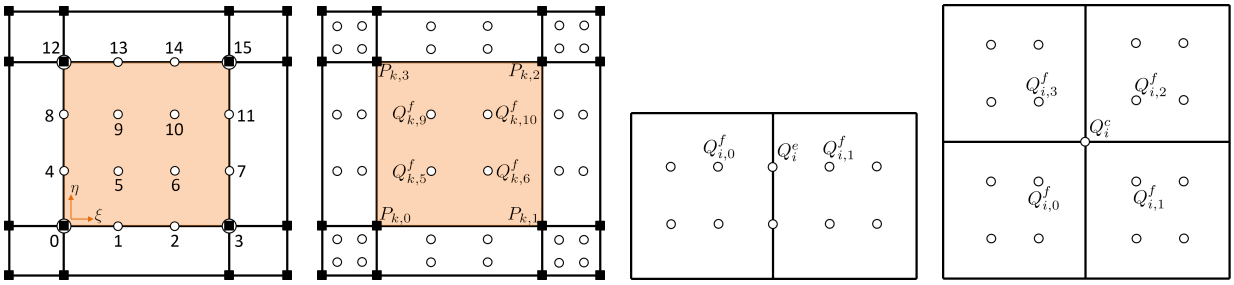


Figure 3: Bézier extraction in 2D for a regular element (shaded orange). (a) The 16 Bézier control points (open circles) determined from the local mesh (black squares), and face points (b), edge points (c) and corner points (d).

We start with an introduction to Bézier extraction on a regular element and later extend the idea to irregular and boundary elements. As shown in Fig. 3(a), Bézier extraction for a regular element $\Omega_k$ (shaded orange) involves calculating 16 Bézier control points (open circles) from the vertices (black squares) of its local mesh $\mathcal{M}_k$. These 16 Bézier control points can be divided into three categories: face points $Q^f_{k,i}$ ($i \in \{5,6,9,10\}$), edge points $Q^e_{k,i}$ ($i \in \{1,2,4,7,8,11,13,14\}$) and corner points $Q^c_{k,i}$ ($i \in \{0,3,12,15\}$). Face points are calculated as a convex combination of four vertices of $\Omega_k$, as shown in Fig. 3(b). We have

$$\mathbf{Q}^f_k = \begin{bmatrix} Q^f_{k,5} \\ Q^f_{k,6} \\ Q^f_{k,10} \\ Q^f_{k,9} \end{bmatrix} = \begin{bmatrix} a & b & c & b \\ b & a & b & c \\ c & b & a & b \\ b & c & b & a \end{bmatrix} \begin{bmatrix} P_{k,0} \\ P_{k,1} \\ P_{k,2} \\ P_{k,3} \end{bmatrix} = \mathbf{M}^f_k \mathbf{P}_k \tag{3}$$

where $a = 4/9$, $b = 2/9$, and $c = 1/9$ are coefficients obtained from the knot insertion algorithm [1] for

uniform knot vectors. Face points are calculated for each element in the local mesh $\mathcal{M}_k$. We have

$$\mathbf{Q}^f = \mathbf{M}^f \mathbf{P}, \tag{4}$$

where $\mathbf{Q}^f$ is the vector of all the face points in $\mathcal{M}_k$, $\mathbf{P}$ is the vector of all the vertices in $\mathcal{M}_k$, and $\mathbf{M}^f$ is assembled from $\mathbf{M}_k^f$ (Eq. (3)). For uniform knot vectors, edge and corner points are then calculated as an average of their neighboring face points. In Fig. 3(c), the edge point $Q_i^e$ is calculated as

$$Q_i^e = \frac{1}{2}\left(Q_{i,0}^f + Q_{i,1}^f\right), \tag{5}$$

where $Q_{i,0}^f$ and $Q_{i,1}^f$ are the two neighboring face points with respect to $Q_i^e$, and the subscripts $(i,0)$ and $(i,1)$ indicate their indices in $\mathbf{Q}^f$. Likewise in Fig. 3(d), the corner point $Q_i^c$ is obtained by

$$Q_i^c = \frac{1}{n}\sum_{j=0}^{n-1} Q_{i,j}^f, \tag{6}$$

where we have valence $n = 4$ in the regular case.

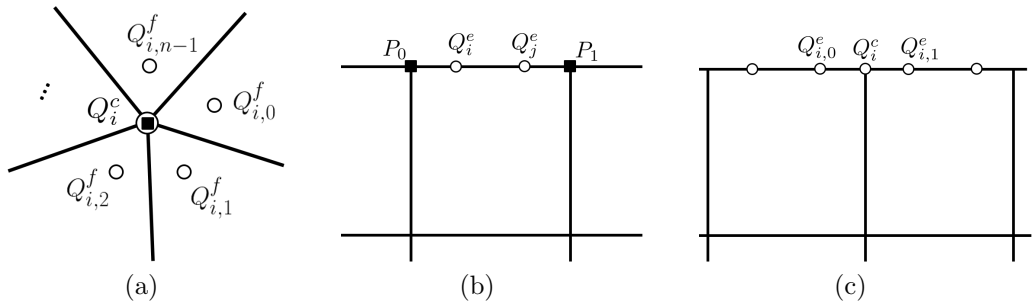


Figure 4: Calculation of a corner point corresponding to an extraordinary vertex (a), edge points corresponding to a boundary edge (b), and corner points corresponding to a boundary vertex (c).

We next study Bézier extraction for an interior irregular element. Compared to Bézier extraction of a regular element, the only difference occurs in the calculation of a corner point. In this case we still use Eq. (6), but $n \neq 4$; see Fig. 4(a). Obviously, Bézier extraction for a regular element is a special case of that for an irregular element. Regarding Bézier extraction for a boundary element, we compute edge/corner Bézier points corresponding to a boundary edge/vertex by treating it as the 1D Bézier extraction for a cubic B-spline curve. As shown in Fig. 4(b), two edge points ($Q_i^e$ and $Q_j^e$) are calculated as convex combinations of two endpoints ($P_0$ and $P_1$) of the edge, and we have

$$\begin{bmatrix} Q_i^e \\ Q_j^e \end{bmatrix} = \begin{bmatrix} 2/3 & 1/3 \\ 1/3 & 2/3 \end{bmatrix} \begin{bmatrix} P_0 \\ P_1 \end{bmatrix}. \tag{7}$$

We have two different ways to compute a boundary corner point, depending on desired continuity for the boundary curve across the corner point. When $C^2$ continuity is desired, the corner point is calculated as an average of its two neighboring boundary edge points; see Fig. 4(c). Otherwise, when $C^0$ is intended (e.g. sharp features), the corner point is set as the corresponding vertex.

From Eqs. (4), (5) and (6), we can observe that all the 16 Bézier points of $\Omega_k$, denoted by $\mathbf{Q}^0$, can be obtained from the face points $\mathbf{Q}^f$ in $\mathcal{M}_k$, and also from the mesh vertices $\mathbf{P}$. We have

$$\mathbf{Q}^0 = \mathbf{M}^a \mathbf{Q}^f = \mathbf{M}^a \mathbf{M}^f \mathbf{P} = \mathbf{M}\mathbf{P}, \tag{8}$$

where $\mathbf{M}^a$ is filled with the coefficients (1 for face points, 1/2 for edge points, and $1/n$ for corner points) in Eqs. (5) and (6) by taking averages of neighboring face points, and $\mathbf{M} = \mathbf{M}^a\mathbf{M}^f$ is called the Bézier

extraction matrix. Note that Eqs. (4), (5) and (6) cannot be immediately extended to polynomial degrees other than the cubic case. Based on Eq. (8), we can derive three types of control meshes from an input quad mesh:

- A *vertex-based control mesh* formed by the input mesh vertices ($\mathbf{P}$), e.g., black squares in Fig. 3(a);
- A *face-point-based control mesh* formed by the face points ($\mathbf{Q}^f$) from Eq. (4) to each element, e.g., open circles in Fig. 3(b); and
- A *Bézier control mesh* formed by all the Bézier points ($\mathbf{Q}^0$) of each element, e.g., open circles in Fig. 3(a).

We next introduce three types of basis functions associated with these three types of control meshes: *vertex-associated functions* $\mathbf{B}^v(\xi,\eta)$, *face-point-associated functions* $\mathbf{B}^f(\xi,\eta)$ and *Bézier functions* $\mathbf{B}^0(\xi,\eta)$ (note that Bézier functions are merely $C^0$ B-splines). Given an element (regular or irregular), $\mathbf{B}^v(\xi,\eta)$ can be represented by linear combinations of $\mathbf{B}^0(\xi,\eta)$ through the transpose of the Bézier extraction matrix $\mathbf{M}$. Without loss of generality, we assume each element is locally parameterized on a unit square $[0,1]^2$, and we have

$$\mathbf{B}^v(\xi,\eta) = \mathbf{M}^T\mathbf{B}^0(\xi,\eta), \quad \mathbf{B}^0(\xi,\eta) = [B_0^0(\xi,\eta), B_1^0(\xi,\eta), \ldots, B_{15}^0(\xi,\eta)]^T, \tag{9}$$

where

$$B_i^0(\xi,\eta) = b_{i\%4}(\xi)b_{i/4}(\eta), \quad i = 0,1,\ldots,15. \tag{10}$$

Here "%" represents "modulo" and "/" stands for "integer division by." $b_j(t)$ $(j = 0,\ldots,3)$ are univariate cubic Bernstein polynomials,

$$b_0(t) = (1-t)^3,\ b_1(t) = 3(1-t)^2t,\ b_2(t) = 3(1-t)t^2,\ b_3(t) = t^3. \tag{11}$$

Face-point-associated functions $\mathbf{B}^f(\xi,\eta)$ can also be represented by $\mathbf{B}^0(\xi,\eta)$ via the transpose of $\mathbf{M}^a$, and we have

$$\mathbf{B}^f(\xi,\eta) = (\mathbf{M}^a)^T\mathbf{B}^0(\xi,\eta). \tag{12}$$

Moreover, $\mathbf{B}^v(\xi,\eta)$ can also be expressed by linear combinations of $\mathbf{B}^f(\xi,\eta)$ via the transpose of $\mathbf{M}^f$, and we have

$$\mathbf{B}^v(\xi,\eta) = (\mathbf{M}^f)^T\mathbf{B}^f(\xi,\eta). \tag{13}$$

Note that on a regular element, $\mathbf{B}^v(\xi,\eta)$ and $\mathbf{B}^f(\xi,\eta)$ are simply $C^2$ and $C^1$ B-splines, respectively, but they are only $C^0$-continuous in irregular elements. Corresponding to Eqs. (9), (12) and (13), we have three pairs of parent-child relationships. A Bézier function $B_j^0$ is called a *Bézier child* of a vertex-associated function $B_i^v$ (or a face-point-associated function $B_i^f$) if the $i$-th row and $j$-th column element of $\mathbf{M}^T$ (or $(\mathbf{M}^a)^T$) is nonzero. Likewise, a face-point-associated function $B_j^f$ is a *face-point-associated child* of a vertex-associated function $B_i^v$ if the $i$-th row and $j$-th column element of $(\mathbf{M}^f)^T$ is nonzero.

In Eqs. (9) and (12), we can observe that each vertex-associated (or face-point-associated) function is uniquely determined by a row of coefficients in $\mathbf{M}^T$ (or $(\mathbf{M}^f)^T$), which are referred to as the *ordinates* of the vertex-associated (or face-point-associated) function. We illustrate the ordinates of several vertex-associated and face-point-associated functions defined on a regular element (shaded orange) in Figs. 5 and 6, respectively. In Fig. 5(a−c), we show the ordinates of three vertex-associated functions $\mathbf{B}^v(\xi,\eta)$ (the black square) in terms of Bézier functions $\mathbf{B}^0(\xi,\eta)$ (open circles). These $\mathbf{B}^v(\xi,\eta)$ are uniform $C^2$ B-splines since the element is regular. A vertex-associated function $B_i^v(\xi,\eta)$ can also be written as a linear combination of the face-point-associated functions $\mathbf{B}^f(\xi,\eta)$ in its one-ring neighborhood; see the corresponding ordinates in Fig. 5(d), where open circles represent face points. In Fig. 6(a), $\mathbf{B}^f(\xi,\eta)$ with support on a given regular element (shaded orange) are marked with green filled circles, whereas those marked with black open circles have no support on the orange element. Due to symmetry, we show the ordinates of three $\mathbf{B}^f(\xi,\eta)$ (green filled circles) in Fig. 6(b−d), respectively, where open circles indicate Bézier points. These $\mathbf{B}^f(\xi,\eta)$ are $C^1$ B-splines on the regular element.

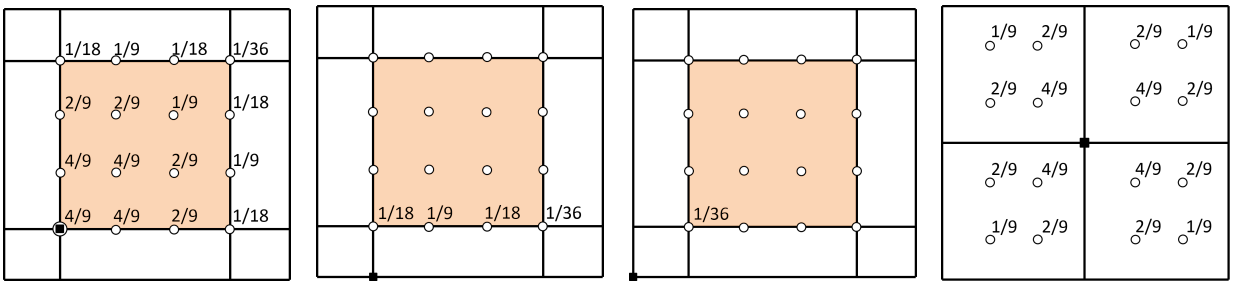


Figure 5: On a regular element (shaded orange), vertex-associated functions $\mathbf{B}^v(\xi,\eta)$ are expressed as linear combinations of Bézier functions $\mathbf{B}^0(\xi,\eta)$ (a–c) and of face-point-associated functions $\mathbf{B}^f(\xi,\eta)$ (d). The black squares represent $\mathbf{B}^v(\xi,\eta)$ of interest. The open circles indicate Bézier points in (a–c) and represent face points in (d).

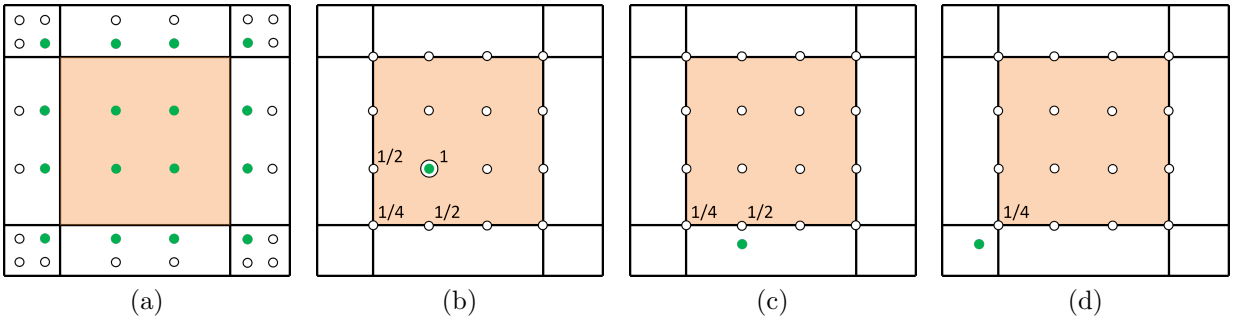


Figure 6: On a regular element (shaded orange), face-point-associated functions $\mathbf{B}^f(\xi,\eta)$ are expressed as linear combinations of Bézier functions $\mathbf{B}^0(\xi,\eta)$. (a) face-point-associated functions $\mathbf{B}^f(\xi,\eta)$ (green filled circles) with support on the element shaded orange, and (b–d) the ordinates of three $\mathbf{B}^f(\xi,\eta)$.

Through Bézier extraction of an element $\Omega_k$, we have three equivalent representations for the same surface patch $S_k(\xi,\eta)$: (1) the *vertex-based representation* with the local mesh and the vertex-associated functions $\mathbf{B}^v(\xi,\eta)$, (2) the *face-point-based representation* with the face points and the face-point-associated functions $\mathbf{B}^f(\xi,\eta)$, and (3) the *Bézier representation* with the Bézier control points and the associated Bézier functions $\mathbf{B}^0(\xi,\eta)$. According to Eqs. (4), (8), (9), (12) and (13), we have the following equivalent relationships,

$$S(\xi,\eta) = \mathbf{P}^T\mathbf{B}^v(\xi,\eta) = (\mathbf{Q}^f)^T\mathbf{B}^f(\xi,\eta) = (\mathbf{Q}^0)^T\mathbf{B}^0(\xi,\eta). \tag{14}$$

Note that even though the face points stay the same in the face-point-based and Bézier representations, their associated basis functions are different. In the face-point-based representation, a face-point-associated function can be represented as a linear combination of $\mathbf{B}^0(\xi,\eta)$; see Fig. 6(b) for example, whereas in the Bézier representation, the basis function associated with a face point is merely a Bézier function.

In summary, for each element in an unstructured quad mesh, all its 16 Bézier points can be calculated from vertices of the local mesh through the Bézier extraction matrix. Three equivalent representations are available through Bézier extraction and have been utilized in the literature. The vertex-based representation was used for all the elements in [23, 34, 31], while the face-point-based representation was adopted in [17]. In [27, 26], the face-point-based representation was adopted around extraordinary vertices whereas the vertex-based representation was used for the remaining regular region. A global Bézier representation is not favored because it introduces a large number of DOF.

### *2.3. Bézier Extraction on Unstructured Hex Meshes*

Similar to Section 2.2, we first introduce several necessary terminologies in an unstructured hex mesh. An unstructured hex mesh consists of vertices (i.e., control points), edges, faces and volumes. Its boundary

is a closed surface or unstructured quad mesh. The number of elements sharing an edge/vertex is called the *valence* of the edge/vertex, respectively. An interior edge with valence other than four, or a boundary edge of valence other than two or one is called an *extraordinary edge*. Endpoints of an extraordinary edge are *extraordinary vertices*. A boundary element is an element with at least one vertex lying on the boundary, and otherwise it is an interior element. An interior element is called an irregular element if any of its vertices is an extraordinary vertex. Otherwise it is a regular element. Since extraordinary vertices may also lie on the boundary, we treat all the boundary elements as irregular elements to simplify the implementation. Bézier extraction for an element involves its local (control) mesh, which is formed by the element and its one-ring neighboring elements. Uniform knot vectors are also assumed here.

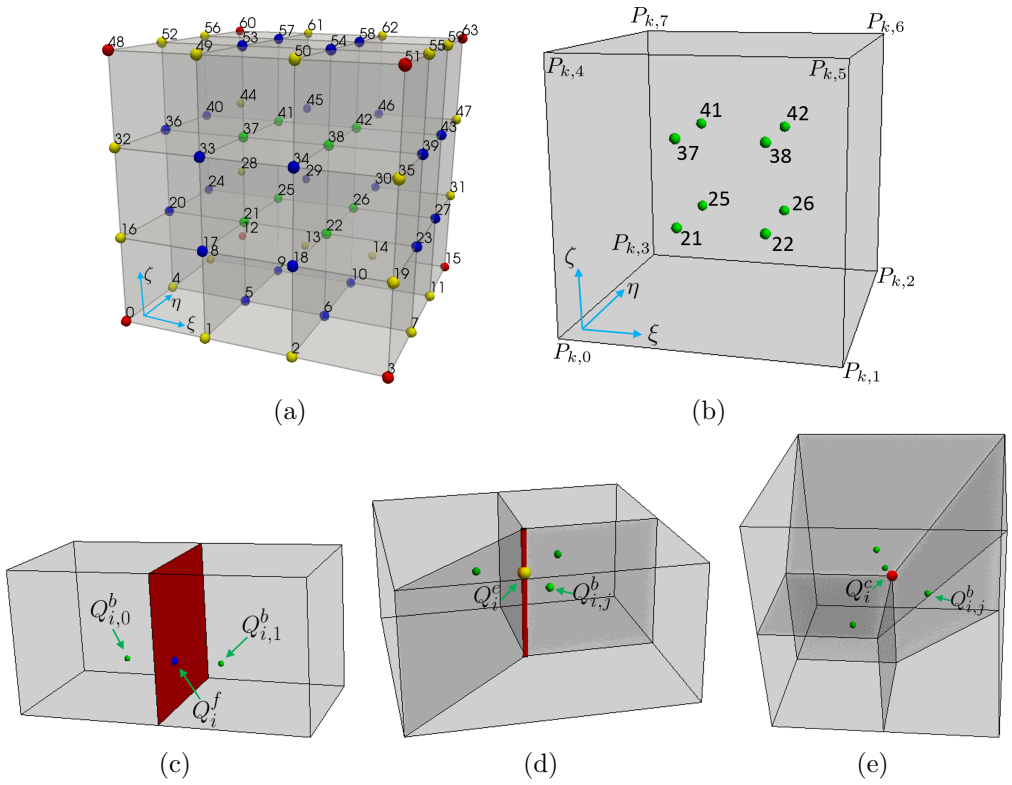


Figure 7: Calculation of Bézier control points for an interior hex element. (a) Locally labeled 64 Bézier points, (b) computing each body point (8 green circles) as a convex combination of eight vertices of this element, (c) computing each face point (the blue circle) as the average of its neighboring body points (green circles), (d) computing each edge point (the yellow circle) as the average of its neighboring body points (green circles), and (e) computing each corner point (the red circle) as the average of its neighboring body points (green circles).

Bézier extraction for a hex element $\Omega_k$ involves computing 64 Bézier control points from the local mesh $\mathcal{M}_k$. The element $\Omega_k$ can be regular or irregular. These Bézier control points are locally labeled in Fig. 7(a) and can be divided into body points $Q_i^b$, face points ($Q_i^f$), edge points ($Q_i^e$), and corner points ($Q_i^c$). Each body point is computed as a convex combination of eight vertices $(P_{k,0}, \ldots, P_{k,7})$ of $\Omega_k$; see Fig. 7(b).

We have

$$\mathbf{Q}_k^b = \begin{bmatrix} Q_{k,21}^b \\ Q_{k,22}^b \\ Q_{k,26}^b \\ Q_{k,25}^b \\ Q_{k,37}^b \\ Q_{k,38}^b \\ Q_{k,42}^b \\ Q_{k,41}^b \end{bmatrix} = \begin{bmatrix} a & b & c & b & b & c & d & c \\ b & a & b & c & c & b & c & d \\ c & b & a & b & d & c & b & c \\ b & c & b & a & c & d & c & b \\ b & c & d & c & a & b & c & b \\ c & b & c & d & b & a & b & c \\ d & c & b & c & c & b & a & b \\ c & d & c & b & b & c & b & a \end{bmatrix} \begin{bmatrix} P_{k,0} \\ P_{k,1} \\ P_{k,2} \\ P_{k,3} \\ P_{k,4} \\ P_{k,5} \\ P_{k,6} \\ P_{k,7} \end{bmatrix} = \mathbf{M}_k^b \mathbf{P}_k, \tag{15}$$

where

$$a = \frac{8}{27},\ b = \frac{4}{27},\ c = \frac{2}{27},\ d = \frac{1}{27}. \tag{16}$$

These coefficients ($a, b, c$ and $d$) are obtained as a tensor-product extension of those in Eq. (3). Body points need to be computed for all elements in the local mesh $\mathcal{M}_k$ to further compute face/edge/corner points. We have

$$\mathbf{Q}^b = \mathbf{M}^b \mathbf{P}, \tag{17}$$

where $\mathbf{Q}^b$ and $\mathbf{P}$ are the vectors of all the face points and vertices in $\mathcal{M}_k$, respectively, and $\mathbf{M}^b$ is assembled by matrices in Eq. (15). Similar to 2D, we treat interior and boundary elements separately. For a Bézier control point corresponding to an interior face/edge/vertex, it is calculated as an average of neighboring body points. In Fig. 7(c−e), the face point $Q_i^f$, the edge point $Q_i^e$ and the corner point $Q_i^c$ are computed as

$$Q_i^f = \frac{1}{2}\left(Q_{i,0}^b + Q_{i,1}^b\right), \quad Q_i^e = \frac{1}{N_e}\sum_{j=0}^{N_e-1} Q_{i,j}^b, \quad Q_i^c = \frac{1}{N_v}\sum_{j=0}^{N_v-1} Q_{i,j}^b, \tag{18}$$

where the subscripts $(i, j)$ indicate indices of neighboring body points in $\mathbf{Q}^b$, $N_e$ and $N_v$ are the valence of the edge and the vertex, respectively. Note that $N_e = 4$ and $N_v = 8$ hold for a regular element. Summarizing the relationships in Eq. (18) in matrix form, we have

$$\mathbf{Q}^0 = \mathbf{M}^a \mathbf{Q}^b, \tag{19}$$

where $\mathbf{Q}^0$ is the vector of all the 64 Bézier control points in $\Omega_k$, and $\mathbf{M}^a$ is filled with coefficients in Eq. (18) computed by taking an average of neighboring body points, that is, 1 for body points, 1/2 for face points, $1/N_e$ for edge points and $1/N_v$ for corner points. On the other hand, for a Bézier control point corresponding to a boundary face/edge/vertex, it is calculated in the same manner as the Bézier extraction on an unstructured quad mesh; see Section 2.2. To this end, all the 64 Bézier points $\mathbf{Q}^0$ can be obtained from the local mesh through the Bézier extraction matrix $\mathbf{M}$, and we have

$$\mathbf{Q}^0 = \mathbf{M}\mathbf{P} \quad \text{and} \quad \mathbf{M} = \mathbf{M}^a \mathbf{M}^b. \tag{20}$$

Similar to 2D, we also have three types of control meshes, which are formed by input mesh vertices, body points and Bézier points. Correspondingly, we have vertex-associated functions $\mathbf{B}^v(\xi, \eta, \zeta)$, body-point-associated functions $\mathbf{B}^b(\xi, \eta, \zeta)$ and Bézier functions $\mathbf{B}^0(\xi, \eta, \zeta)$ that can be defined on a given element (regular or irregular). $\mathbf{B}^v(\xi, \eta, \zeta)$ can be represented by $\mathbf{B}^b(\xi, \eta, \zeta)$ and $\mathbf{B}^0(\xi, \eta, \zeta)$, and we have

$$\mathbf{B}^v(\xi, \eta, \zeta) = (\mathbf{M}^b)^T \mathbf{B}^b(\xi, \eta, \zeta) = (\mathbf{M}^b)^T (\mathbf{M}^a)^T \mathbf{B}^0(\xi, \eta, \zeta) = \mathbf{M}^T \mathbf{B}^0(\xi, \eta, \zeta), \tag{21}$$

where each Bézier function in $\mathbf{B}^0(\xi, \eta, \zeta)$ is a tensor product of three univariate Bernstein polynomials. $\mathbf{B}^b(\xi, \eta, \zeta)$ can also be represented by linear combinations of $\mathbf{B}^0(\xi, \eta, \zeta)$, and we have

$$\mathbf{B}^b(\xi, \eta, \zeta) = (\mathbf{M}^a)^T \mathbf{B}^0(\xi, \eta, \zeta). \tag{22}$$

Three equivalent representations are also available for each hex element, that is, the vertex-based representation, the body-point-based representation, and the Bézier representation. They have expressions similar to

Eq. (14). Based on Eqs. (21) and (22), we also have three parent-child relationships similar to 2D, but note that we have *body-point-associated children* instead of face-point-associated children for a vertex-associated function.

On a regular element, we show the ordinates of a body-point-associated function, e.g., $Q^b_{k,21}$ in Fig. 7(a). Here we write the ordinates in a list of pairs $(i, c)$, where $c \in \mathbb{R}$ is the ordinate corresponding to the $i$-th $(0 \leq i \leq 63)$ Bézier function. We only list nonzero ordinates, and for the body-point-associated function of $Q^b_{k,21}$, we have $\{(0, 1/8), (1, 1/4), (4, 1/4), (5, 1/2), (16, 1/4), (17, 1/2), (20, 1/2), (21, 1)\}$. For a body-point-associated function defined on an interior irregular element, the ordinate corresponding to an extraordinary edge is simply replaced by $1/N_e$, where $N_e$ is the valence of the extraordinary edge. The same argument applies to the ordinate corresponding to an extraordinary vertex.

Although there are three representations (Eq. (14)) that we can choose from for an unstructured hex mesh, each of them has its own limitations. When either a vertex-based or body-point-based representation is employed, refinement in irregular hex elements cannot preserve the parameterization. Refinement schemes such as Catmull-Clark subdivision do not yield optimal convergence rates [3, 31]. If a global Bézier representation is adopted, an enormous number of DOF needs to be introduced, leading to a huge computation burden for the subsequent refinement. In this paper, we present a blended B-spline construction to achieve optimal convergence rates with minimal extra DOF introduced.

## 3. Blended B-Spline Construction on Unstructured Quad Meshes

In this section, we present a new blended $C^0/C^1/C^2$ B-spline construction method (namely, the $C012$ construction) for unstructured quad meshes. We will extend such blended construction to unstructured hex meshes in Section 4. Recall that we have defined several terminologies for an unstructured quad mesh; see Fig. 2. The entire unstructured quad mesh can be divided into two submeshes: a regular submesh consisting of all regular elements and an irregular submesh consisting of all irregular elements. In Fig. 8(a), the regular and irregular submeshes are shaded orange and blue, respectively. Note that irregular elements also include boundary elements for open surfaces. The interface of these two submeshes is formed by a set of edges and vertices; see the green edges in Fig. 8(a). An element is called a *transition element* if it contains one or more interface vertex. A transition element can be either regular or irregular. There are three steps to construct a blended B-spline representation: (1) adding face points and edge/corner Bézier points to the quad mesh, (2) defining spline functions on each element, and (3) performing truncation for irregular elements and regular transition elements.

**Step 1: Adding face points and edge/corner Bézier points to unstructured quad mesh.** As shown in Fig. 8(a), all the spoke and boundary edges are identified as $C^0$ edges (red edges), whereas all the extraordinary and boundary vertices are identified as $C^0$ vertices (red squares). We first add face points to each irregular element; see the green filled circles in Fig. 8(b). Then, we add Bézier points (red filled circles) to all $C^0$ edges and $C^0$ vertices. In this way, the boundary curve is represented as a piecewise Bézier curve, where the added Bézier points form the control polygon. Extraordinary vertices are allowed on the boundary. In our blended B-spline construction, we do not need to separate adjacent extraordinary vertices in the input mesh. In other words, we allow multiple extraordinary vertices in a single element. Separating extraordinary vertices is usually needed in isogeometric spline forests [24], which involves global refinement of the input mesh and thus introduces a large number of unnecessary DOF. Although such separation can be handled locally, it still needs to modify the input mesh [30]. In contrast, our blended method adds explicit functions without modifying the input mesh, which significantly simplifies the implementation, especially for 3D.

**Step 2: Defining spline functions on each element.** There are three types of spline functions defined on an element: vertex-associated functions $B^v_i$, face-point-associated functions $B^f_j$ and Bézier functions $B^0_k$. In the input quad mesh, each vertex is associated with a $B^v_i$ with support over its two-ring neighborhood. Each face point is associated with a $B^f_j$ with influence on its one-ring neighboring elements. Each edge/corner Bézier point is associated with a $B^0_k$, which only has support on elements sharing it. To

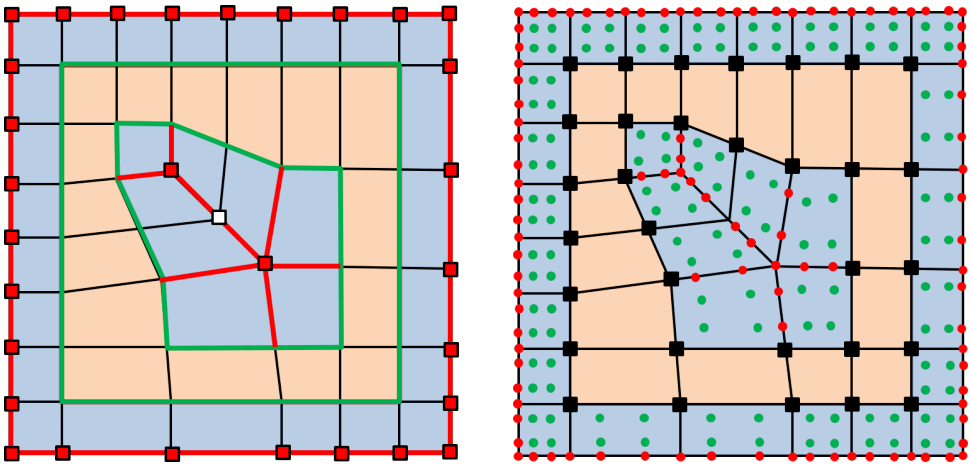

(a) (b)

Figure 8: Adding face points and edge/corner Bézier points to an unstructured quad mesh. (a) The input unstructured quad mesh with regular elements (orange), irregular elements (blue), the interface (green edges), $C^0$ edges (red edges) and $C^0$ vertices (red squares), and (b) adding face points (green filled circles) and edge/corner Bézier points (red filled circles) on $C^0$ edges/vertices, respectively. The black filled squares represent active vertices, whereas all the other mesh vertices are passive.

ensure linear independence, we distinguish active and passive functions and only adopt active ones in our blended construction. A vertex-associated function $B_i^v$ is *passive* if all its one-ring neighboring elements are irregular. Otherwise it is *active*. The associated vertex is also said to be active or passive. All the added face points and edge/corner Bézier points in Step 1 are active. This can be verified by checking a vertex with all irregular one-ring neighboring elements, where we need to add face points accordingly and its associated $B_i^v$ can be represented as a linear combination of these active face-point-associated functions. To ensure linear independence, we cannot adopt this $B_i^v$ in our blended construction and thus it is passive. According to this definition, the vertex-associated function of any extraordinary vertex or boundary vertex is also passive. A regular vertex may also be passive; see the black open square in Fig. 8(a) as an example. In Fig. 8(b), only the black squares are associated with active vertex-associated functions, whereas all the other mesh vertices are passive.

Next we discuss how to define these three types of spline functions on an element. The key idea is to check if any of these functions has support on the element. According to the support of involved functions, it suffices to loop through elements in its local mesh and check all the active mesh vertices as well as face points and edge/corner Bézier points. There are a total of four types of elements: regular non-transition element, irregular non-transition element, regular transition element and irregular transition element. A regular non-transition element, whose local mesh only contains regular elements, only has vertex-associated functions $B_i^v$ defined on it, and these $B_i^v$ are simply uniform $C^2$ B-splines. The local mesh of an irregular non-transition element only contains irregular elements, so face-point-associated functions $B_j^f$ and Bézier functions $B_k^0$ are defined on such an element. On the other hand, there exist both regular and irregular elements in the local mesh of a transition element. We have vertex-associated functions $B_i^v$ and face-point-associated functions $B_j^f$ defined on a regular transition element, where all active $B_i^v$ are uniform $C^2$ B-splines and all $B_j^f$ are $C^1$ B-splines. In contrast, all three types of functions ($B_i^v$, $B_j^f$, $B_k^0$) are defined on an irregular transition element; see blue elements in Fig. 8(b). We summarize in Table 1 the types of spline functions defined on these four different types of elements.

**Step 3: Performing truncation on irregular elements and regular transition elements.** After the above two steps, in the blended construction we need to guarantee that neighboring surface patches join one another seamlessly. This can be achieved by employing the truncation mechanism [12] in irregular elements and regular transition elements, where different types of functions are blended together. The

Table 1: Possible splines functions defined on different types of quad elements

| Element type | vertex-associated functions $B_i^v$ | face-point-associated functions $B_j^f$ | Bézier functions $B_k^0$ |
|---|---|---|---|
| Regular non-transition | Yes | No | No |
| Irregular non-transition | No | Yes | Yes |
| Regular transition | Yes | Yes | No |
| Irregular transition | Yes | Yes | Yes |

truncation mechanism was originally developed in the context of hierarchical B-splines to reduce support overlapping of basis functions and thus to yield sparser stiffness matrices. Later this idea was extended to Catmull-Clark subdivision functions [32, 33], T-splines [34], and hierarchical splines on unstructured hex meshes [31]. The essential idea of the truncation mechanism is to discard repeated contributions of active children basis functions. In the following, we explain how to perform the truncation mechanism in our blended B-spline construction.

Recall that according to Eqs. (12), (9) and (13), we have defined Bézier children of a face-point-associated function as well as Bézier children and face-point-associated children of a vertex-associated function $B_i^v$. Performing truncation on a $B_i^v$ (or a face-point-associated function $B_j^f$) is to set the ordinates of its active children to be zero. Correspondingly, we have one type of truncation for $B_j^f$ and two types of truncation for $B_i^v$. In Fig. 9(a), we start with the truncation of a generic $B_j^f$ (the green filled circle) as an example, where $a$, $b$ and $c$ are its ordinates and they vary in different elements. These three ordinates correspond to three Bézier points (red open circles). $B_j^f$ needs a truncation when any of these three Bézier points is active. Note that active Bézier points correspond to $C^0$ edges/vertices only, where $C^0$ tags are assigned to extraordinary vertices, spoke edges as well as boundary edges and boundary vertices, so this type of truncation is always needed in irregular elements. Fig. 9(b−f) show all the possible cases of truncated $B_j^f$, where only red filled circles are active Bézier points. Particularly in Fig. 9(f), all three ordinates are zero. In such case, $B_j^f$ degenerates to a Bézier function. In Fig. 10(a) and (b), we also show contour plots of $B_j^f$ corresponding to Fig. 9(c) before and after truncation, respectively. We can observe $C^0$ continuity across element boundaries after truncating $B_j^f$.

Instead of distinguishing different cases as in Fig. 9, in practice truncation is performed elementwise by manipulating related matrices. For an element $\Omega_k$, we first express the parent-child relationship in Eq. (12) by distinguishing active and passive[2] Bézier functions ($\mathbf{B}_a^0$ and $\mathbf{B}_p^0$, respectively). We have

$$\mathbf{B}^f = \begin{bmatrix} \mathbf{B}_a^f \\ \mathbf{B}_p^f \end{bmatrix} = (\mathbf{M}^a)^T \mathbf{B}^0 = \begin{bmatrix} (\mathbf{M}_{aa}^a)^T & (\mathbf{M}_{ap}^a)^T \\ (\mathbf{M}_{pa}^a)^T & (\mathbf{M}_{pp}^a)^T \end{bmatrix} \begin{bmatrix} \mathbf{B}_a^0 \\ \mathbf{B}_p^0 \end{bmatrix}, \tag{23}$$

where $\mathbf{B}_a^f$ and $\mathbf{B}_p^f$ are active and passive face-point-associated functions, respectively. Performing truncation is equivalent to setting the submatrices $(\mathbf{M}_{aa}^a)^T = \mathbf{0}$ and $(\mathbf{M}_{pa}^a)^T = \mathbf{0}$. Thus we obtain truncated face-point-associated functions $\mathbf{B}_t^f$ on $\Omega_k$

$$\mathbf{B}_t^f = \begin{bmatrix} \mathbf{B}_{a,t}^f \\ \mathbf{B}_{p,t}^f \end{bmatrix} = \begin{bmatrix} \mathbf{0} & (\mathbf{M}_{ap}^a)^T \\ \mathbf{0} & (\mathbf{M}_{pp}^a)^T \end{bmatrix} \begin{bmatrix} \mathbf{B}_a^0 \\ \mathbf{B}_p^0 \end{bmatrix} = \begin{bmatrix} (\mathbf{M}_{ap}^a)^T \\ (\mathbf{M}_{pp}^a)^T \end{bmatrix} \mathbf{B}_p^0. \tag{24}$$

We next study the truncation for an active vertex-associated function $B_i^v$, which must be associated with an interior regular vertex. Similar to truncating a face-point-associated function, we set the ordinates corresponding to active children to be zero. We first introduce the truncation of $B_i^v$ with respect to face-point-associated children. Recall that in Fig. 5(d), $B_i^v$ (associated with the black square) can be represented

[2]Passive face-point-associated functions and passive Bézier functions only serve an auxiliary purpose to explain the truncation mechanism and they are not used in a blended construction.

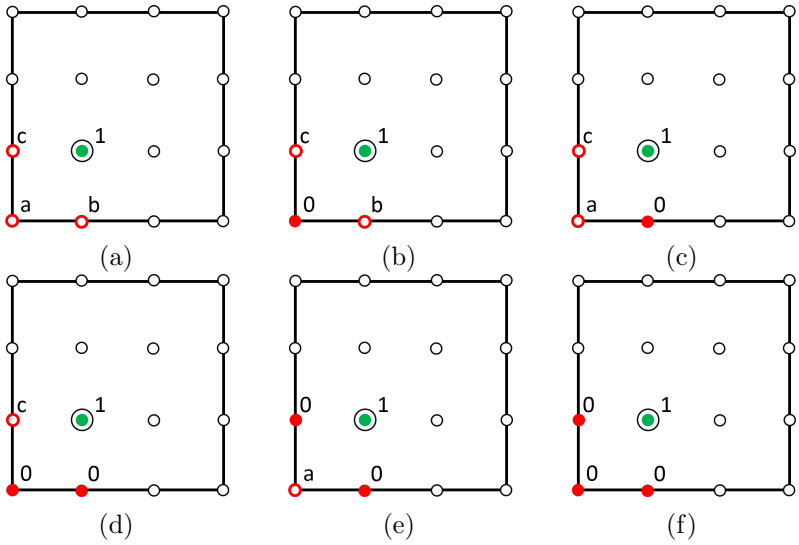


Figure 9: Truncation of a generic face-point-associated function $B_j^f$ (green filled circles). (a) The ordinates of $B_j^f$, where three of its Bézier children (red open circles) may be active, and (b−f) five possible configurations of active Bézier points (red filled circles).

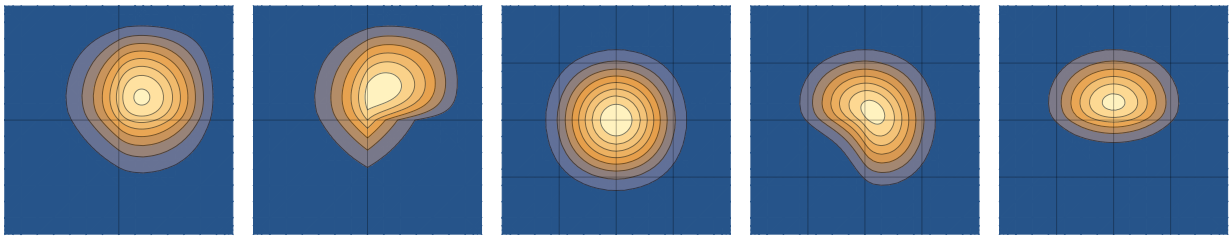


Figure 10: (a, b) Contour plots of a face-point-associated function $B_j^f$ corresponding to Fig. 9(c) before and after truncation, (c) the contour plot of a vertex-associated function $B_i^v$, and (d, e) contour plots of truncated $B_i^v$ corresponding to Fig. 11(a, b), respectively.

by a linear combination of its 16 face-point-associated children (open circles), which are located within its one-ring neighborhood. If any element in the one-ring neighborhood is irregular, then all its four face-point-associated children are active. We truncate $B_i^v$ by setting the ordinates corresponding to these face-point-associated children as zero. We show all possible configurations of such a truncation in Fig. 11, where irregular elements are shaded blue, and green filled circles and black open circles represent active and passive face-point-associated children, respectively. Particularly in Fig. 11(e), all the one-ring neighboring elements are irregular and all the ordinates become zero, leading to $B_i^v$ zero. Recall that we set such a $B_i^v$ to be passive and do not use it in the blended construction. Also note that all the active $B_i^v$ (black squares) need to be truncated in Fig. 8(b). In Fig. 10(c−e), we show contour plots of a $B_i^v$ before and after truncation. Fig. 10(c) shows $B_i^v$ before truncation, whereas Fig. 10(d, e) shows two examples of truncation corresponding to Fig. 11(a, b), respectively.

Fig. 11 is used to illustrate how the truncation mechanism works. In practice, we only need to deal with related matrices during truncation. Rewriting Eq. (13) by distinguishing active and passive face-point-associated functions $\mathbf{B}^f$, we have

$$\mathbf{B}^v = \begin{bmatrix} (\mathbf{M}_a^f)^T & (\mathbf{M}_p^f)^T \end{bmatrix} \begin{bmatrix} \mathbf{B}_a^f \\ \mathbf{B}_p^f \end{bmatrix}. \tag{25}$$

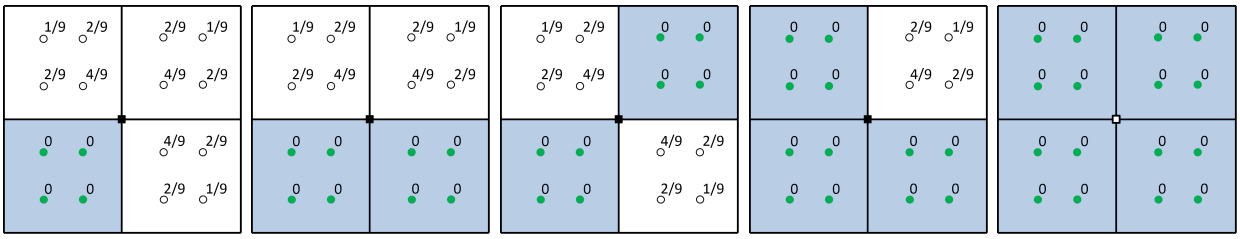


Figure 11: Truncation of a vertex-associated function $B_i^v$ (the black filled or open square) with different configurations of irregular elements in the one-ring neighborhood. Green filled circles and black open circles are associated with active and passive face-point-associated functions $B_j^f$, respectively. Black filled squares represent active $B_i^v$, whereas the black open square represents passive $B_i^v$.

Since in the end we prefer to expressing every function in terms of Bézier functions $\mathbf{B}^0$, we further replace $\mathbf{B}^f$ with $\mathbf{B}^0$ via Eq. (23). Eq. (25) becomes

$$\mathbf{B}^v = \begin{bmatrix}(\mathbf{M}_a^f)^T & (\mathbf{M}_p^f)^T\end{bmatrix}(\mathbf{M}^a)^T\mathbf{B}^0 = \begin{bmatrix}(\mathbf{M}_a^f)^T & (\mathbf{M}_p^f)^T\end{bmatrix}\begin{bmatrix}(\mathbf{M}_{aa}^a)^T & (\mathbf{M}_{ap}^a)^T\\ (\mathbf{M}_{pa}^a)^T & (\mathbf{M}_{pp}^a)^T\end{bmatrix}\begin{bmatrix}\mathbf{B}_a^0\\ \mathbf{B}_p^0\end{bmatrix}. \tag{26}$$

We set $(\mathbf{M}_a^f)^T = \mathbf{0}$ when truncating $\mathbf{B}^v$ with respect to face-point-associated children, and $(\mathbf{M}_{aa}^a)^T = \mathbf{0}$ and $(\mathbf{M}_{pa}^a)^T = \mathbf{0}$ when truncating $\mathbf{B}^f$ with respect to Bézier children; see Eq. (24). After truncating $\mathbf{B}^v$ in Eq. (26), we obtain

$$\mathbf{B}_t^v = \begin{bmatrix}\mathbf{0} & (\mathbf{M}_p^f)^T\end{bmatrix}\begin{bmatrix}\mathbf{0} & (\mathbf{M}_{ap}^a)^T\\ \mathbf{0} & (\mathbf{M}_{pp}^a)^T\end{bmatrix}\begin{bmatrix}\mathbf{B}_a^0\\ \mathbf{B}_p^0\end{bmatrix} = (\mathbf{M}_p^f)^T(\mathbf{M}_{pp}^a)^T\mathbf{B}_p^0. \tag{27}$$

Likewise, the truncation of $\mathbf{B}^v$ with respect to their Bézier children is performed by setting their corresponding ordinates to be zero. Actually this type of truncation has been included in Eq. (27), where the truncated vertex-associated functions $\mathbf{B}_t^v$ are only expressed in terms of passive Bézier functions $\mathbf{B}_p^0$. Based on Table 1, we list the types of truncation involved in different elements in Table 2.

Table 2: Truncation types in different elements

| Element type | Truncating $\mathbf{B}^v$ w.r.t. face-point-associated children | Truncating $\mathbf{B}^v$ w.r.t. Bézier children | Truncating $\mathbf{B}^f$ w.r.t. Bézier children |
|---|---|---|---|
| Regular non-transition | No | No | No |
| Irregular non-transition | No | No | Yes |
| Regular transition | Yes | No | No |
| Irregular transition | Yes | No | Yes |

To this end, we have defined spline functions on each element in an unstructured quad mesh. Each spline function is represented as a linear combination of Bézier functions $\mathbf{B}^0$, with certain ordinates set to zero when truncation is needed. Without loss of generality, we write spline functions $\mathbf{B}$ defined on an irregular transition element as

$$\mathbf{B} = \begin{bmatrix}\mathbf{B}_t^v\\ \mathbf{B}_{a,t}^f\\ \mathbf{B}_a^0\end{bmatrix} = \begin{bmatrix}\mathbf{0} & (\mathbf{M}_p^f)^T(\mathbf{M}_{pp}^a)^T\\ \mathbf{0} & (\mathbf{M}_{ap}^a)^T\\ \mathbf{I} & \mathbf{0}\end{bmatrix}\begin{bmatrix}\mathbf{B}_a^0\\ \mathbf{B}_p^0\end{bmatrix} = \mathbf{T}\mathbf{B}^0, \tag{28}$$

where $\mathbf{I}$ is an identity matrix and $\mathbf{T}$ is the Bézier extraction matrix in the blended construction. Note that for convenience we include all the vertex-associated functions, where a passive vertex-associated function simply has all its ordinates equal to zero. The surface patch corresponding to this irregular transition

element is represented by

$$S(\xi,\eta)=\mathbf{P}_{\text{all}}^{T}\mathbf{B}=\begin{bmatrix}\mathbf{P}^{T} & (\mathbf{Q}_{a}^{f})^{T} & (\mathbf{Q}_{a}^{0})^{T}\end{bmatrix}\begin{bmatrix}\mathbf{B}_{t}^{v}\\ \mathbf{B}_{a,t}^{f}\\ \mathbf{B}_{a}^{0}\end{bmatrix}, \tag{29}$$

where $\mathbf{P}$, $\mathbf{Q}_a^f$ and $\mathbf{Q}_a^0$ are mesh vertices, active face points and active edge/corner Bézier points, respectively. Eq. (29) is called the *blended geometric representation*. The blended geometric representation is $C^2$-continuous in the regular region, $C^1$-continuous across the interface between regular and irregular regions, and $C^0$-continuous in the irregular region. Eqs. (28) and (29) indicate a unified manner for all types of elements. This unified representation significantly simplifies the implementation, where we only need to distinguish regular and irregular elements together with the truncation as a separate operation. Note that for the same element, the geometric representations in Eqs. (29) and (14) are equivalent, which will be proved in Section 5.

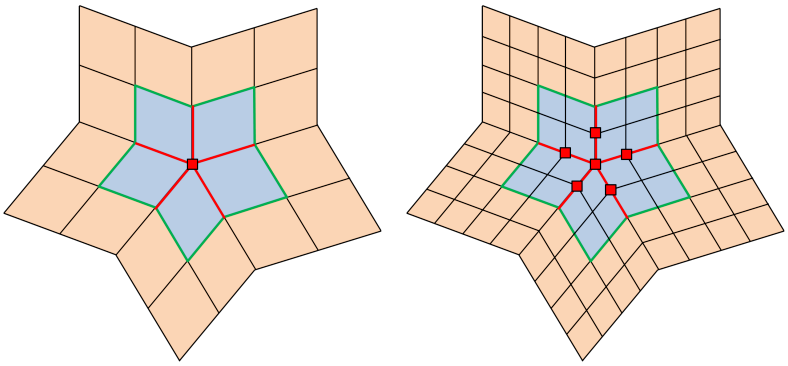

(a) Given mesh (b) Refined mesh

Figure 12: Refinement of elements around an extraordinary vertex, with regular and irregular elements shaded orange and blue, respectively. Red squares and red edges represent $C^0$ vertices and $C^0$ edges, respectively. Green edges represent the interface between regular and irregular elements.

The purpose of building spline functions in such a blended manner is to keep consistent parameterization during refinement. This property will be proved in Section 5. We here focus on how to perform refinement in a blended construction. We first introduce how vertices and Bézier points are updated during refinement, and then discuss how spline functions are defined on the refined mesh. Overall, the knot insertion algorithm [1, 19] is used for refinement of all types of elements. According to Eqs. (14) and (29), we have four equivalent geometric representations for each element. In refinement, we switch the blended representation to the vertex-based representation for a regular element (i.e., uniform B-splines), whereas we adopt the Bézier representation for an irregular element. Applying the knot insertion algorithm to a Bézier patch is equivalent to performing the de Casteljau's algorithm [2]. By refinement, a regular surface patch results in four uniform B-spline subpatches, whereas a Bézier patch is subdivided into four Bézier subpatches. All the involved vertices and Bézier points are updated in the same manner following the classical knot insertion algorithm. Regarding defining spline functions on the refined mesh, we only need to discuss how irregular elements and $C^0$ edges/vertices are updated. Spline functions can be defined in the same way by following the three-step construction. The key idea of passing irregular elements and $C^0$ information to refined meshes is to maintain the continuity across initial spoke edges during refinement. We refine elements by splitting them into $2\times 2$ sub-elements. Topologically, this implies that each vertex in the coarse mesh remains the same in the refined mesh, and each edge is split into two sub-edges with one new regular vertex inserted in the middle. All the four sub-elements of an irregular element still remain irregular. Recall that in the input mesh, spoke edges, boundary edges, extraordinary vertices and boundary vertices are identified with $C^0$ tags. After refinement, the sub-edges of a $C^0$ edge remain $C^0$, whereas newly added edges are not $C^0$ edges. The midpoint of a $C^0$ edge is also marked as a $C^0$ vertex. All the $C^0$ vertices stay with $C^0$ tags during

refinement. By recursively updating irregular elements, $C^0$ edges and $C^0$ vertices, we always maintain $C^0$ continuity during refinement across the spoke edges in the input mesh. This is critical in preserving consistent parameterization as well as achieving optimal convergence rates. Given a submesh around an extraordinary vertex (the red square) in Fig. 12(a), after refinement $C^0$ edges and $C^0$ vertices are updated in Fig. 12(b), which are marked as red edges and red squares, respectively. Regular and irregular elements are shaded orange and blue, respectively, and their interface is represented by green edges.

**Discussion 3.1.** Unstructured quad/hex meshes generally involve boundary extraordinary vertices, where several additional layers of elements need to be created before open knot vectors can be used. In our blended construction, instead of adopting open knot vectors, we treat boundary elements as irregular elements. In this manner, we do not need to modify the input mesh and thus can simplify the implementation.

**Discussion 3.2.** Truncation plays the key role in a blended B-spline construction. It reduces the support of certain face-point-associated and vertex-associated functions, and ends up with a set of truncated functions that form a partition of unity. Truncated vertex-associated functions (or truncated face-point-associated functions) are equivalent to truncated $C^2$ B-splines (or truncated $C^1$ B-splines). In other words, truncation removes "irregular" child functions from vertex-associated and face-point-associated functions. Essentially, we blend $C^0$ B-splines and truncated $C^1/C^2$ B-splines together to form a basis. It enables a seamless transition from the irregular submesh to the regular submesh, and provides us the flexibility to blend different types of spline functions. "Flexibility" here means that we can design various blended constructions with different properties. One can easily switch to another blended construction by slightly modifying Step 1. The above discussed blended construction blends $C^0$, truncated $C^1$ and truncated $C^2$ B-splines, so we refer to it as the $C012$ *construction*. It provides a $C^1$ smooth transition from the irregular submesh to the regular submesh, but with only global linear independence. Two alternative blended constructions are given in Appendix A, where more Bézier functions are added to the interface of the irregular and regular submeshes to ensure local linear independence, leading to a $C^0$ transition across the interface. These two alternatives are called the $C02$ construction and the $C02i$ construction. The $C02$ *construction* only blends vertex-associated functions and Bézier functions, where all the Bézier points are added in irregular elements in the input mesh as well as subsequent refined meshes. As an improvement of the $C02$ construction, the $C02i$ *construction* introduces face-point-associated functions within each irregular element in refined meshes and thus yields fewer DOF. For easy comparison, Fig. 13 shows how face points and edge/corner Bézier points are added to the same irregular elements after refinement under these three constructions. Details can be found in Appendix A. In all three constructions ($C012$, $C02$ and $C02i$), spline functions form a partition of unity, are globally linearly independent, and preserve consistent parameterization during refinement. These properties will be proved under the $C012$ construction in Section 5. The proofs under the other two constructions are very similar. We list several different properties in Table 3 for easy reference.

Table 3: Additional properties in different blended constructions

| Construction type | Linear independence | $C^1$ smooth transition | Number of DOF |
|---|---|---|---|
| $C012$ | Global | Yes | + |
| $C02$ | Local | No | +++ |
| $C02i$ | Local | No | ++ |

Note: More "+" means more DOF.

**Discussion 3.3.** Refinement schemes for unstructured quad meshes with $C^1$ continuity are available in [20, 17, 27]. However, to the best of our knowledge, extending such refinement schemes to unstructured hex meshes is far from a trivial task. Focusing only on quad meshes, $C^1$ and $C^2$ functions are blended in [27] by properly scaling certain $C^1$ functions. In [26], an intermediate $C^0$ space is constructed for unstructured quad meshes using face-point-associated functions with necessary Bézier functions; this space is later modified into a $C^1$ space. In contrast, in this paper we use not only face-point-associated and Bézier functions, but also vertex-associated functions to reduce the number of DOF, which is beneficial especially in 3D. Moreover, we introduce the truncation mechanism to conveniently blend these three types of functions, such that it can

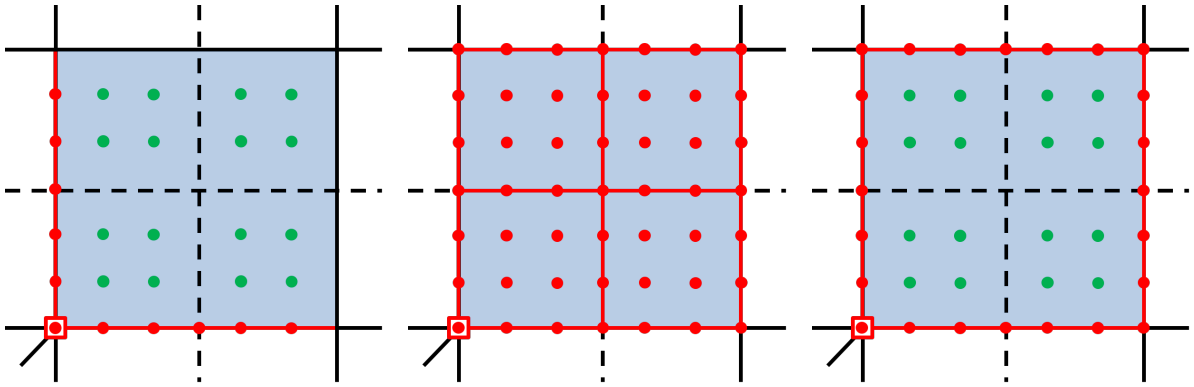

(a) $C012$ (b) $C02$ (c) $C02i$

Figure 13: Adding face points (green filled circles) and Bézier points (red filled circles) to irregular elements (shaded blue) after refinement under different constructions. The solid black lines represent the mesh before refinement, and dashed black lines indicate refinement. Red edges are $C^0$ edges after refinement. The red open square is an extraordinary vertex.

be straightforwardly extended to unstructured hex meshes.

## 4. Blended B-spline Construction on Unstructured Hex Meshes

Following the construction idea of unstructured quad meshes, in this section we extend our discussion to unstructured hex meshes. In addition to the notations we have introduced in Section 2.3, we here introduce several more as an extension from 2D. An unstructured hex mesh is decomposed into a *regular submesh* and an *irregular submesh*, which contain regular and irregular elements, respectively. The interface of these two submeshes consists of a set of faces, edges and vertices. An *interface face* must be shared by two elements, one being regular and the other being irregular. Elements containing one or more interface vertices are *transition elements*, which can be either regular or irregular. Similar to 2D, there are three steps in our blended B-spline construction for unstructured hex meshes: (1) adding body points and face/edge/corner Bézier points to the hex mesh, (2) identifying spline functions with support on each element, and (3) performing truncation for irregular elements and regular transition elements. The main difference from 2D lies in Step 1.

In Step 1, $C^0$ tags are assigned to extraordinary vertices, extraordinary edges, spoke faces and boundary faces/edges/vertices in the input mesh. A *spoke face* is a face touching an extraordinary edge. Body points are added to each irregular element, and Bézier points are added to faces, edges and vertices with $C^0$ tags. An irregular element is shown in Fig. 14(a) with one of its edges being an extraordinary edge (marked in red). According to the definition, its two endpoints are extraordinary vertices (black circles) and two faces (shaded dark grey) sharing the extraordinary edge are spoke faces. In Fig. 14(b), the added face points and face/edge/corner Bézier points are marked with green and red circles, respectively. We show two examples in Fig. 14(c, d) explaining how Bézier points are added to a spoke face, where red edges and red open squares represent extraordinary edges and extraordinary vertices, respectively. A spoke face may have other configurations of extraordinary edges, where Bézier points can be added analogously.

The next two steps are very similar to those in 2D. In Step 2, given an element $\Omega_k$, we loop through all the elements in its local mesh and collect active vertex-associated functions $B_i^v$, body-point-associated functions $B_j^b$ as well as Bézier functions $B_k^0$. A $B_i^v$ is passive if all of its one-ring neighboring elements are irregular. Regarding types of spline functions defined on different elements, we can obtain similar results as Table 1 in 2D, where we only need to change "face-point-associated functions $B_j^f$" to "body-point-associated functions $B_j^b$." In Fig. 15, we use three configurations to show neighboring $B_j^b$ with support on an element of interest (orange elements). A neighboring element (shaded grey) may share a face (Fig. 15(a)), an edge (Fig. 15(b)), or a vertex (Fig. 15(c)) with the orange element. If a neighboring element is irregular, eight $B_j^b$

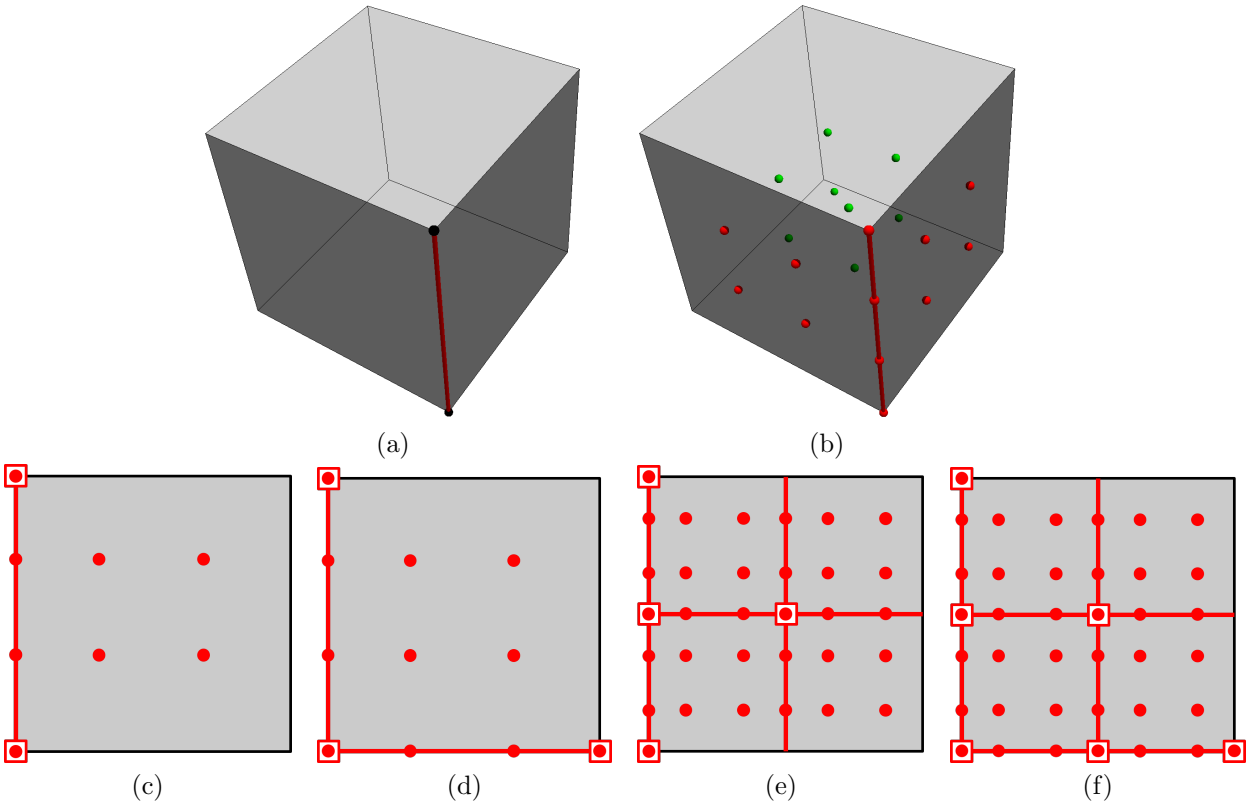


Figure 14: (a) An irregular element with an extraordinary edge (the red edge) and two extraordinary vertices (black circles), (b) adding body points (green circles) and face/edge/corner Bézier points (red circles) to the element in (a), (c, d) two examples of adding Bézier points (red circles) to spoke faces, and (e, f) adding Bézier points to $C^0$ faces after refining the spoke faces in (c, d), respectively. Spoke faces and $C^0$ faces are shaded dark grey in (a, b). In (c−f), $C^0$ edges and $C^0$ vertices are represented by red edges and red open squares, respectively.

(green circles and black circles) are added. However, only those associated with green circles have support on the orange element.

In Step 3, following the same manner as in 2D, we perform three types of truncation in irregular elements and regular transition elements: body-point-associated functions $B_j^b$ with respect to Bézier children, and vertex-associated functions $B_i^v$ with respect to body-point-associated or Bézier children. By truncation, we set ordinates corresponding to active children to be zero. In Fig. 16(a), we first show the truncation for $B_j^b$ (the green circle), which has eight Bézier children (black circles in Fig. 16(b)). We assume that the red edge in Fig. 16(c) is an extraordinary edge, so two faces (dark grey) touching it are spoke faces. Due to the presence of this extraordinary edge, four active Bézier points (red circles) are added, whose corresponding ordinates are set to be zero when truncating $B_j^b$ (the green circle). Truncating $B_i^v$ with respect to body-point-associated children is a direct extension from 2D, where we only need to check if there exists any irregular element in its one-ring neighborhood. Truncating $B_i^v$ with respect to Bézier children is straightforward and has been included when performing the other two types of truncation. Eq. (28) also works for truncation in 3D, where we replace "$\mathbf{B}_{a,t}^f$" with "$\mathbf{B}_{a,t}^b$" and replace "$\mathbf{M}_p^f$" with "$\mathbf{M}_p^b$."

To this end, we have built spline functions on the input unstructured hex mesh. Next we discuss how to perform refinement. It is a tensor-product extension from 2D, where a regular volume patch is refined in the same way as a tricubic uniform B-spline and an irregular patch employs the de Casteljau's algorithm for a tricubic Bézier patch. Similar to 2D, tracking $C^0$ tags is still the key to maintain $C^0$ continuity across the initial spoke faces during refinement. A hex element is subdivided into 8 sub-elements with one center vertex, 6 edges and 12 faces generated in the interior. All the sub-elements of an irregular element are

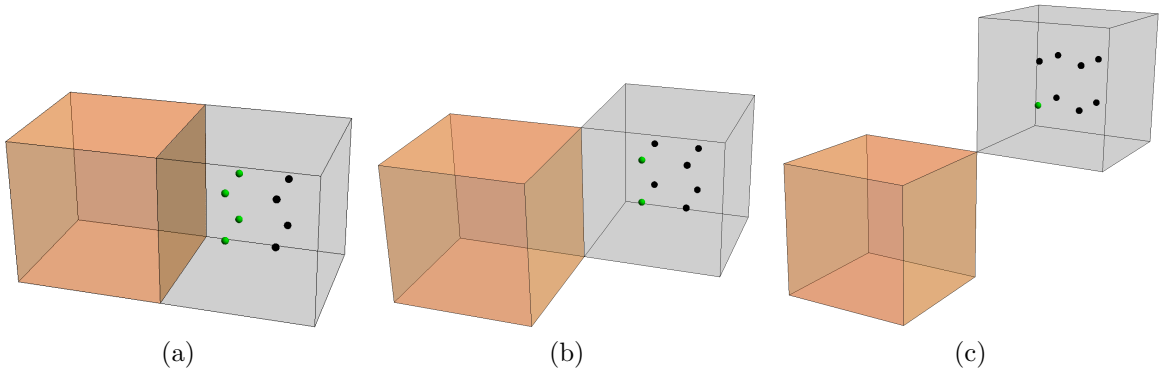


Figure 15: Three different configurations of neighboring body-point-associated functions $B_j^b$ with support on an element of interest (shaded orange). Neighboring irregular elements are shaded grey. Only those $B_j^b$ associated with green circles have support on the orange element.

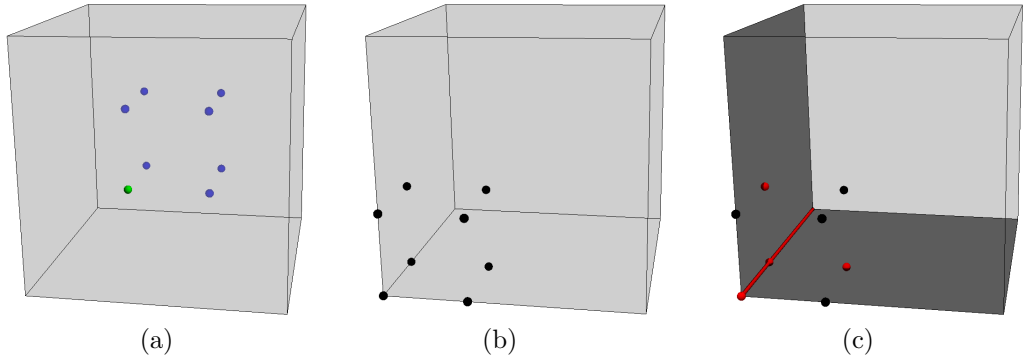


Figure 16: Truncation of a body-point-associated function $B_i^v$ with respect to active Bézier children. (a) A body-point-associated function $B_j^b$ of interest (the green circle), (b) the eight Bézier children (black circles) of $B_j^b$, and (c) active Bézier children (red circles) due to presence of an extraordinary edge (the red edge) and two spoke faces (dark grey faces).

tagged "irregular," although some of them do not have any extraordinary edge. Sub-faces of a $C^0$ face and sub-edges of a $C^0$ edge inherit $C^0$ tags. The newly generated center vertex and four edges of a $C^0$ face as well as the middle vertex of a $C^0$ edge are also tagged $C^0$. The given $C^0$ vertices stay the same. In Fig. 14(e, f), we show two cases how $C^0$ tags are assigned after refining a spoke face in Fig. 14(c, d), respectively. $C^0$ faces/edges/vertices are denoted by grey shade, red edges and red open squares, respectively.

**Discussion 4.1.** The truncation mechanism provides a convenient way to seamlessly connect regular and irregular patches, where we only need to manipulate the Bézier extraction matrix $\mathbf{T}$ in Eq. (28). Although T-spline local knot vectors can be used as well in 2D to connect regular and irregular patches [30, 4], the underlying mesh needs to be modified by inserting edges around extraordinary vertices. Extending this idea to 3D becomes very difficult due to the complex connectivity of an unstructured hex mesh.

**Discussion 4.2.** The vertex-based representation is employed for every hex element for truncated hierarchical splines in [31], with the solid Catmull-Clark subdivision rule [5] used for refinement. A suboptimal convergence behavior was observed. Special treatment is also needed to construct hierarchical splines due to the lack of refinability. Refinability can be enabled in our blended construction but requires enlargement of the irregular region as well as assigning $C^0$ tags to additional faces/edges/vertices at each refinement step. We postpone the detailed discussion as part of our future work in the context of hierarchical refinement.

## 5. Properties of Blended B-Spline Construction

In this section, we prove several important properties under the $C012$ blended B-spline construction, including partition of unity, consistent parameterization, and global linear independence. These properties are also possessed in the other two constructions (the $C02$ construction and the $C02i$ construction) and they can be proved in a similar manner. Local linear independence is a property only available in the $C02$ and $C02i$ constructions, which will be discussed in Appendix A. We here start with the proof of partition of unity.

**Proposition 1.** *Spline functions in the $C012$ blended B-spline construction form a non-negative partition of unity.*

*Proof.* We prove this proposition elementwise. Recall that Eq. (28) is a unified expression of spline functions defined on all types of elements and it is also generic in both 2D and 3D, and we have $\mathbf{B} = \mathbf{T}\mathbf{B}^0$ where

$$\mathbf{T} = \begin{bmatrix} \mathbf{0} & (\mathbf{M}_p^f)^T(\mathbf{M}_{pp}^a)^T \\ \mathbf{0} & (\mathbf{M}_{ap}^a)^T \\ \mathbf{I} & \mathbf{0} \end{bmatrix}. \tag{30}$$

Spline functions in $\mathbf{B}$ are non-negative because all entries in the Bézier extraction matrix $\mathbf{T}$ are non-negative. The next step is to prove splines functions in $\mathbf{B}$ form a partition of unity. With Bézier functions $\mathbf{B}^0$ forming a partition of unity, we only need to verify that each column sum of $\mathbf{T}$ equals 1.0. Any column sum of the identity matrix is one, so we only need to verify each column sum of the remaining two submatrices, $(\mathbf{M}_p^f)^T(\mathbf{M}_{pp}^a)^T$ and $(\mathbf{M}_{ap}^a)^T$. Note that in 3D, $\mathbf{M}_p^b$ is used instead of $\mathbf{M}_p^f$. We define

$$\mathbf{M}_1 := \begin{bmatrix} \mathbf{0} & (\mathbf{M}_p^f)^T \\ \mathbf{I} & \mathbf{0} \end{bmatrix} \tag{31}$$

and

$$\mathbf{M}_2 := \mathbf{M}_1(\mathbf{M}^a)^T = \begin{bmatrix} \mathbf{0} & (\mathbf{M}_p^f)^T \\ \mathbf{I} & \mathbf{0} \end{bmatrix} \begin{bmatrix} (\mathbf{M}_{aa}^a)^T & (\mathbf{M}_{ap}^a)^T \\ (\mathbf{M}_{pa}^a)^T & (\mathbf{M}_{pp}^a)^T \end{bmatrix} = \begin{bmatrix} (\mathbf{M}_p^f)^T(\mathbf{M}_{pa}^a)^T & (\mathbf{M}_p^f)^T(\mathbf{M}_{pp}^a)^T \\ (\mathbf{M}_{aa}^a)^T & (\mathbf{M}_{ap}^a)^T \end{bmatrix}. \tag{32}$$

Each column sum of $(\mathbf{M}_p^f)^T$ equals 1.0 because its transpose $\mathbf{M}_p^f$ is used to compute passive face points as convex combinations[3] of element corners. Therefore, each column sum of $\mathbf{M}_1$ is 1.0. Similarly, each column sum of $(\mathbf{M}^a)^T$ equals 1.0 since $\mathbf{M}^a$ is used to compute face/edge/corner Bézier points as convex combinations of neighboring face (or body) points. We can then easily obtain that each column sum of their multiplication $\mathbf{M}_2$ also equals 1.0. Comparing $\mathbf{T}$ and $\mathbf{M}_2$ in Eqs. (30) and (32) especially their second columns, we can conclude that each column sum of $\mathbf{T}$ is also 1.0. Therefore, spline functions in the $C012$ blended construction form a non-negative partition of unity.

□

To prove consistent parameterization during refinement, we need the following lemma to assist the proof.

**Lemma 1.** *In the $C012$ blended B-spline construction, the blended geometric representation for any element is equivalent to the vertex-based representation.*

*Proof.* We prove elementwise that the blended geometric representation $\mathbf{P}_{\text{all}}^T\mathbf{B}$ in Eq. (29), which is generic in 2D and 3D, is equivalent to the vertex-based representation $\mathbf{P}^T\mathbf{B}^v$. Given an element of any type, we start from its vertex-based representation $\mathbf{P}^T\mathbf{B}^v$ and express the vertex-associated functions $\mathbf{B}^v$ in terms of active and passive face-point-associated (or body-point-associated) children according to Eq. (25). We have

$$\mathbf{P}^T\mathbf{B}^v = \mathbf{P}^T \begin{bmatrix} (\mathbf{M}_a^f)^T & (\mathbf{M}_p^f)^T \end{bmatrix} \begin{bmatrix} \mathbf{B}_a^f \\ \mathbf{B}_p^f \end{bmatrix} = \begin{bmatrix} (\mathbf{M}_a^f\mathbf{P})^T & (\mathbf{M}_p^f\mathbf{P})^T \end{bmatrix} \begin{bmatrix} \mathbf{B}_a^f \\ \mathbf{B}_p^f \end{bmatrix} = \begin{bmatrix} (\mathbf{Q}_a^f)^T & (\mathbf{Q}_p^f)^T \end{bmatrix} \begin{bmatrix} \mathbf{B}_a^f \\ \mathbf{B}_p^f \end{bmatrix}, \tag{33}$$

[3] A convex combination is defined to be a linear combination where all the coefficients are non-negative and their sum equals 1.0.

where $\mathbf{Q}_a^f = \mathbf{M}_a^f\mathbf{P}$ and $\mathbf{Q}_p^f = \mathbf{M}_p^f\mathbf{P}$. $\mathbf{Q}_a^f$ and $\mathbf{Q}_p^f$ are active and passive face points, respectively. Note that the notation "$\mathbf{M}_a^f$" is replaced by "$\mathbf{M}_a^b$" in 3D. We further substitute face-point-associated functions ($\mathbf{B}_a^f$ and $\mathbf{B}_p^f$) with Bézier functions ($\mathbf{B}_a^0$ and $\mathbf{B}_p^0$) according to Eq. (23). We have

$$\begin{aligned}\mathbf{P}^T\mathbf{B}^v =& \begin{bmatrix}(\mathbf{Q}_a^f)^T & (\mathbf{Q}_p^f)^T\end{bmatrix}\begin{bmatrix}(\mathbf{M}_{aa}^a)^T & (\mathbf{M}_{ap}^a)^T\\ (\mathbf{M}_{pa}^a)^T & (\mathbf{M}_{pp}^a)^T\end{bmatrix}\begin{bmatrix}\mathbf{B}_a^0\\ \mathbf{B}_p^0\end{bmatrix}\\ =&(\mathbf{M}_{aa}^a\mathbf{Q}_a^f + \mathbf{M}_{pa}^a\mathbf{Q}_p^f)^T\mathbf{B}_a^0 + (\mathbf{M}_{ap}^a\mathbf{Q}_a^f + \mathbf{M}_{pp}^a\mathbf{Q}_p^f)^T\mathbf{B}_p^0\\ =&(\mathbf{M}_{aa}^a\mathbf{Q}_a^f + \mathbf{M}_{pa}^a\mathbf{Q}_p^f)^T\mathbf{B}_a^0 + (\mathbf{Q}_a^f)^T(\mathbf{M}_{ap}^a)^T\mathbf{B}_p^0 + \mathbf{P}^T(\mathbf{M}_p^f)^T(\mathbf{M}_{pp}^a)^T\mathbf{B}_p^0.\end{aligned} \tag{34}$$

From Eq. (8), we have $\mathbf{Q}_a^0 = \mathbf{M}_{aa}^a\mathbf{Q}_a^f + \mathbf{M}_{pa}^a\mathbf{Q}_p^f$, where $\mathbf{Q}_a^0$ represent active Bézier points. From Eq. (28), we have $\mathbf{B}_t^v = (\mathbf{M}_p^f)^T(\mathbf{M}_{pp}^a)^T\mathbf{B}_p^0$ and $\mathbf{B}_{a,t}^f = (\mathbf{M}_{ap}^a)^T\mathbf{B}_p^0$. Therefore, Eq. (34) becomes

$$\mathbf{P}^T\mathbf{B}^v = (\mathbf{Q}_a^0)^T\mathbf{B}_a^0 + (\mathbf{Q}_a^f)^T\mathbf{B}_{a,t}^f + \mathbf{P}^T\mathbf{B}_t^v = \begin{bmatrix}\mathbf{P}^T & (\mathbf{Q}_a^f)^T & (\mathbf{Q}_a^0)^T\end{bmatrix}\begin{bmatrix}\mathbf{B}_t^v\\ \mathbf{B}_{a,t}^f\\ \mathbf{B}_a^0\end{bmatrix}. \tag{35}$$

Comparing Eqs. (35) and (29), we can easily obtain $\mathbf{P}^T\mathbf{B}^v = \mathbf{P}_{\text{all}}^T\mathbf{B}$. This concludes that the blended representation is equivalent to the vertex-based representation.

□

Due to the equivalence of three representations (Eq. (14)), Lemma 1 also indicates that the blended representation is equivalent to the Bézier representation as well as the face-point-based (or body-point-based) representation. We are now ready to prove consistent parameterization during refinement with the aid of Lemma 1.

**Proposition 2.** *The parameterization corresponding to any element in the $C$012 blended B-spline construction stays the same during refinement.*

*Proof.* We here use 2D terminologies (e.g., "the face-point-based representation") for explanation, but all arguments also apply to 3D (e.g., "the body-point-based representation") with a straightforward tensor-product extension. We first discuss how to obtain face points around the interface between regular and irregular submeshes during refinement, which is critical to the following proof. Due to their equivalence (a direct result of Lemma 1), we switch the blended representation to the face-point-based representation. All the face-point-associated functions with support on the interface are actually $C^1$ B-splines $\mathbf{B}_{\text{int}}^f$, so the interface is represented by $(\mathbf{Q}_{\text{int}}^f)^T\mathbf{B}_{\text{int}}^f$, where $\mathbf{Q}_{\text{int}}^f$ are corresponding face points of $\mathbf{B}_{\text{int}}^f$. We perform refinement by applying the knot insertion algorithm [1] to these $C^1$ B-splines $\mathbf{B}_{\text{int}}^f$. After refinement, the interface is represented by $(\tilde{\mathbf{Q}}_{\text{int}}^f)^T\tilde{\mathbf{B}}_{\text{int}}^f$, where "$\sim$" denotes refinement, $\tilde{\mathbf{B}}_{\text{int}}^f$ are refined $C^1$ B-splines with support on the interface, and $\tilde{\mathbf{Q}}_{\text{int}}^f$ are their corresponding face points obtained through the knot insertion algorithm. We have $(\mathbf{Q}_{\text{int}}^f)^T\mathbf{B}_{\text{int}}^f = (\tilde{\mathbf{Q}}_{\text{int}}^f)^T\tilde{\mathbf{B}}_{\text{int}}^f$ restricted on the interface. An interface edge (the red edge) is shown in Fig. 17 with the dashed line indicating refinement, where $\mathbf{Q}_{\text{int}}^f$ and $\tilde{\mathbf{Q}}_{\text{int}}^f$ are marked with green open circles and green filled circles, respectively. We next show that refinement in the blended construction can yield the same refined face points $\tilde{\mathbf{Q}}_{\text{int}}^f$. An interface edge is shared by two transition elements, one being regular and the other being irregular; see the orange and blue elements in Fig. 17. In the blended construction, a regular transition element is refined by applying the knot insertion algorithm to its uniform $C^2$ B-spline control mesh $\mathbf{P}$, whereas an irregular element is refined by applying the de Casteljau algorithm to its corresponding Bézier control mesh $\mathbf{Q}^0$. This yields a refined uniform B-spline mesh $\tilde{\mathbf{P}}$ and a refined Bézier control mesh $\tilde{\mathbf{Q}}^0$. Since essentially only classical $C^1$ B-spline functions are involved on the interface, the face points calculated using the refined B-spline mesh $\tilde{\mathbf{P}}$ via Eqs. (3) and (15) stay the same with $\tilde{\mathbf{Q}}_{\text{int}}^f$, and the face Bézier points in $\tilde{\mathbf{Q}}^0$ also coincide with $\tilde{\mathbf{Q}}_{\text{int}}^f$. In other words, refinement based on different representations can yield the same refined face points $\tilde{\mathbf{Q}}_{\text{int}}^f$ around the interface.

We need to prove consistent parameterization for regular transition elements, irregular non-transition elements and irregular transition elements. It is obvious that consistent parameterization holds for regular

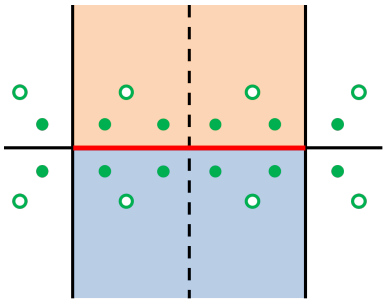

Figure 17: Refinement around an interface edge (the red edge), where solid black lines represent the mesh before refinement and the dashed line indicates refinement. Elements sharing the interface edge are shaded orange and blue, representing a regular element and an irregular element, respectively. Green open circles and green filled circles represent face-point-associated functions with support on the interface edge before and after refinement, respectively.

non-transition elements, where only subdivision of uniform $C^2$ B-splines is involved. Let us first prove the proposition holds for a regular transition element. According to Lemma 1, we switch the blended representation $\mathbf{P}_{\text{all}}^T\mathbf{B}$ to the vertex-based representation $\mathbf{P}^T\mathbf{B}^v$ without changing the geometry. By performing the knot insertion algorithm to uniform $C^2$ B-splines, we have

$$\mathbf{P}_{\text{all}}^T\mathbf{B} = \mathbf{P}^T\mathbf{B}^v = \tilde{\mathbf{P}}^T\tilde{\mathbf{B}}^v, \tag{36}$$

where $\tilde{\mathbf{P}}$ is the refined mesh, $\mathbf{B}^v$ and $\tilde{\mathbf{B}}^v$ are uniform $C^2$ B-splines on a regular element. Analogous to Eq. (25), we write $\tilde{\mathbf{B}}^v$ in terms of its active and passive face-point-associated children (i.e., $C^1$ B-splines here), and we have

$$\tilde{\mathbf{P}}^T\tilde{\mathbf{B}}^v = \tilde{\mathbf{P}}^T\begin{bmatrix}(\tilde{\mathbf{M}}_a^f)^T & (\tilde{\mathbf{M}}_p^f)^T\end{bmatrix}\begin{bmatrix}\tilde{\mathbf{B}}_a^f \\ \tilde{\mathbf{B}}_p^f\end{bmatrix} = (\tilde{\mathbf{M}}_a^f\tilde{\mathbf{P}})^T\tilde{\mathbf{B}}_a^f + \tilde{\mathbf{P}}^T(\tilde{\mathbf{M}}_p^f)^T\tilde{\mathbf{B}}_p^f. \tag{37}$$

We denote $\tilde{\mathbf{Q}}_{a,1}^f := \tilde{\mathbf{M}}_a^f\tilde{\mathbf{P}}$, which represent active face points calculated from the refined mesh $\tilde{\mathbf{P}}$. In the blended construction, active face points must correspond to irregular elements and they are calculated based on the Bézier representation. The associated functions of $\tilde{\mathbf{Q}}_{a,1}^f$ are $C^1$ B-splines with support on the interface. Therefore, $\tilde{\mathbf{Q}}_{a,1}^f$ is a subvector of $\tilde{\mathbf{Q}}_{\text{int}}^f$, and according to our previous discussion we have $\tilde{\mathbf{Q}}_{a,1}^f = \tilde{\mathbf{Q}}_a^f$, where $\tilde{\mathbf{Q}}_a^f$ are obtained based on the Bézier representation. In Fig. 17, $\tilde{\mathbf{Q}}_a^f$ are the green filled circles located within the irregular element (shaded blue). Since no Bézier functions are involved in a regular transition element, we have $(\tilde{\mathbf{M}}_p^f)^T\tilde{\mathbf{B}}_p^f = \tilde{\mathbf{B}}_t^v$, where $\tilde{\mathbf{B}}_t^v$ are truncated vertex-associated functions in the refined mesh. Therefore, Eq. (37) becomes

$$\tilde{\mathbf{P}}^T\tilde{\mathbf{B}}^v = (\tilde{\mathbf{Q}}_a^f)^T\tilde{\mathbf{B}}_a^f + \tilde{\mathbf{P}}^T\tilde{\mathbf{B}}_t^v = \tilde{\mathbf{P}}_{\text{all}}^T\tilde{\mathbf{B}}, \tag{38}$$

which concludes consistent parameterization during refinement on a regular transition element.

Next for an irregular non-transition element, we switch the blended representation $\mathbf{P}_{\text{all}}^T\mathbf{B}$ to the Bézier representation $(\mathbf{Q}^0)^T\mathbf{B}^0$ and perform the de Casteljau algorithm for refinement. We have

$$\mathbf{P}_{\text{all}}^T\mathbf{B} = (\mathbf{Q}^0)^T\mathbf{B}^0 = (\tilde{\mathbf{Q}}^0)^T\tilde{\mathbf{B}}^0, \tag{39}$$

where $\mathbf{B}$ contains (truncated) face-point-associated functions $\mathbf{B}_{a,t}^f$ (i.e., $C^1$ B-splines) and active Bézier functions $\mathbf{B}_a^0$. We only need to show that after refinement, the blended representation can yield the same Bézier points as $\tilde{\mathbf{Q}}^0$, which ensures that the geometry is preserved during refinement in the blended representation. After refinement, the blended representation on an irregular non-transition element is defined as

$$\tilde{\mathbf{P}}_{\text{all}}^T\tilde{\mathbf{B}} = \begin{bmatrix}(\tilde{\mathbf{Q}}_a^f)^T & (\tilde{\mathbf{Q}}_a^0)^T\end{bmatrix}\begin{bmatrix}\tilde{\mathbf{B}}_{a,t}^f \\ \tilde{\mathbf{B}}_a^0\end{bmatrix} = (\tilde{\mathbf{Q}}_a^f)^T\tilde{\mathbf{B}}_{a,t}^f + (\tilde{\mathbf{Q}}_a^0)^T\tilde{\mathbf{B}}_a^0, \tag{40}$$

which is analogous to Eq. (29) after excluding vertex-associated functions $\mathbf{B}_t^v$. According to the definition of truncated face-point-associated functions $\tilde{\mathbf{B}}_{a,t}^f$ in Eq. (24), we substitute $\tilde{\mathbf{B}}_{a,t}^f$ with $(\tilde{\mathbf{M}}_{ap}^a)^T\tilde{\mathbf{B}}_p^0$ and we

have

$$\tilde{\mathbf{P}}_{\text{all}}^T \tilde{\mathbf{B}} = (\tilde{\mathbf{M}}_{ap}^a \tilde{\mathbf{Q}}_a^f)^T \tilde{\mathbf{B}}_p^0 + (\tilde{\mathbf{Q}}_a^0)^T \tilde{\mathbf{B}}_a^0. \tag{41}$$

Note that according to how $C^0$ tags are assigned to the refined mesh, all the passive Bézier points $\tilde{\mathbf{Q}}_p^0$ are calculated only from active face points $\tilde{\mathbf{Q}}_a^f$, leading to $\tilde{\mathbf{M}}_{ap}^a \tilde{\mathbf{Q}}_a^f = \tilde{\mathbf{Q}}_p^0$. Eq. (41) becomes

$$\tilde{\mathbf{P}}_{\text{all}}^T \tilde{\mathbf{B}} = (\tilde{\mathbf{Q}}_p^0)^T \tilde{\mathbf{B}}_p^0 + (\tilde{\mathbf{Q}}_a^0)^T \tilde{\mathbf{B}}_a^0 = (\tilde{\mathbf{Q}}^0)^T \tilde{\mathbf{B}}^0, \tag{42}$$

which concludes consistent parameterization during refinement on an irregular non-transition element.

Finally for an irregular transition element, we also switch to the Bézier representation $(\mathbf{Q}^0)^T \mathbf{B}^0$ for refinement. We have the same expression as in Eq. (39), but note that $\mathbf{B}$ contains all three types of functions on an irregular transition element. We next show that after refinement, the blended construction can yield the same Bézier points as $\tilde{\mathbf{Q}}^0$. Analogous to Eq. (29), on the refined mesh we have the blended representation as

$$\tilde{\mathbf{P}}_{\text{all}}^T \tilde{\mathbf{B}} = \begin{bmatrix} \tilde{\mathbf{P}}^T & (\tilde{\mathbf{Q}}_a^f)^T & (\tilde{\mathbf{Q}}_a^0)^T \end{bmatrix} \begin{bmatrix} \tilde{\mathbf{B}}_t^v \\ \tilde{\mathbf{B}}_{a,t}^f \\ \tilde{\mathbf{B}}_a^0 \end{bmatrix}, \tag{43}$$

where $\tilde{\mathbf{P}}$, $\tilde{\mathbf{Q}}_a^f$ and $\tilde{\mathbf{Q}}_a^0$ are refined mesh vertices, active face points and active edge/corner Bézier points, respectively. According to the proof on an irregular non-transition element, all the Bézier points in $\tilde{\mathbf{Q}}^0$ can be calculated from $\tilde{\mathbf{Q}}_a^f$ and $\tilde{\mathbf{Q}}_a^0$ except those corresponding to the interface (i.e., interface faces/edges/vertices). Restricted on the interface, we only have vertex-associated functions and face-point-associated functions with support on it, so the proof is the same as that on a regular transition element. Indeed, refinement based on different representations yields the same set of face points, which further can yield the same Bézier points corresponding to the interface. This concludes consistent parameterization during refinement on an irregular transition element. To this end, we have proved consistent parameterization for each type of elements.

□

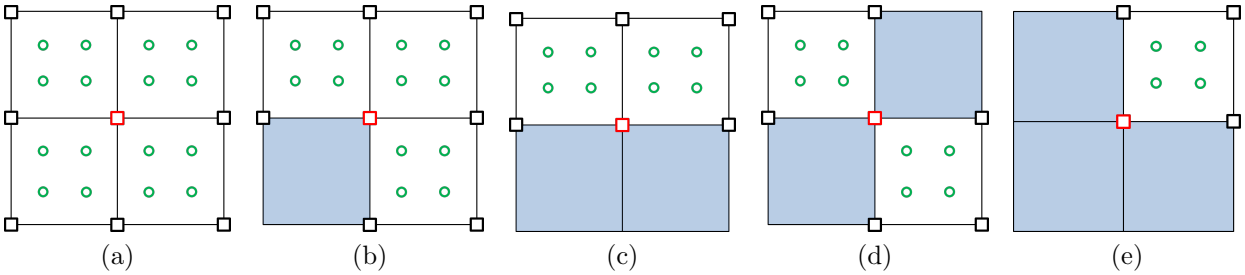


Figure 18: Five possible cases in 2D where linear dependence may occur. $B_{t,i}^v$, $B_{t,j}^v$ and their face-point-associated children in Eq. (44) are associated with the red open square, black open squares and green open circles, respectively. The irregular region is shaded blue. The dimension of the underlying matrix $\mathbf{M}$ in (a−e) is $9 \times 16$, $8 \times 12$, $6 \times 8$, $7 \times 8$ and $4 \times 4$, respectively.

Last but not least, we prove the linear independence of spline functions in the blended construction. In particular, they are globally linearly independent on the entire domain, but may be locally linearly dependent on certain elements individually. In Appendix A, we will discuss local linear independence of two alternative blended constructions.

**Proposition 3.** *The spline functions in the $C012$ blended B-spline construction are linearly independent on the entire domain.*

*Proof.* We use 2D terminologies for explanation, but the arguments are the same in 3D. We first restrict ourselves on the regular subdomain determined by the regular submesh, where only vertex-associated functions and face-point-associated functions have support. These functions are actually uniform $C^2$ B-splines

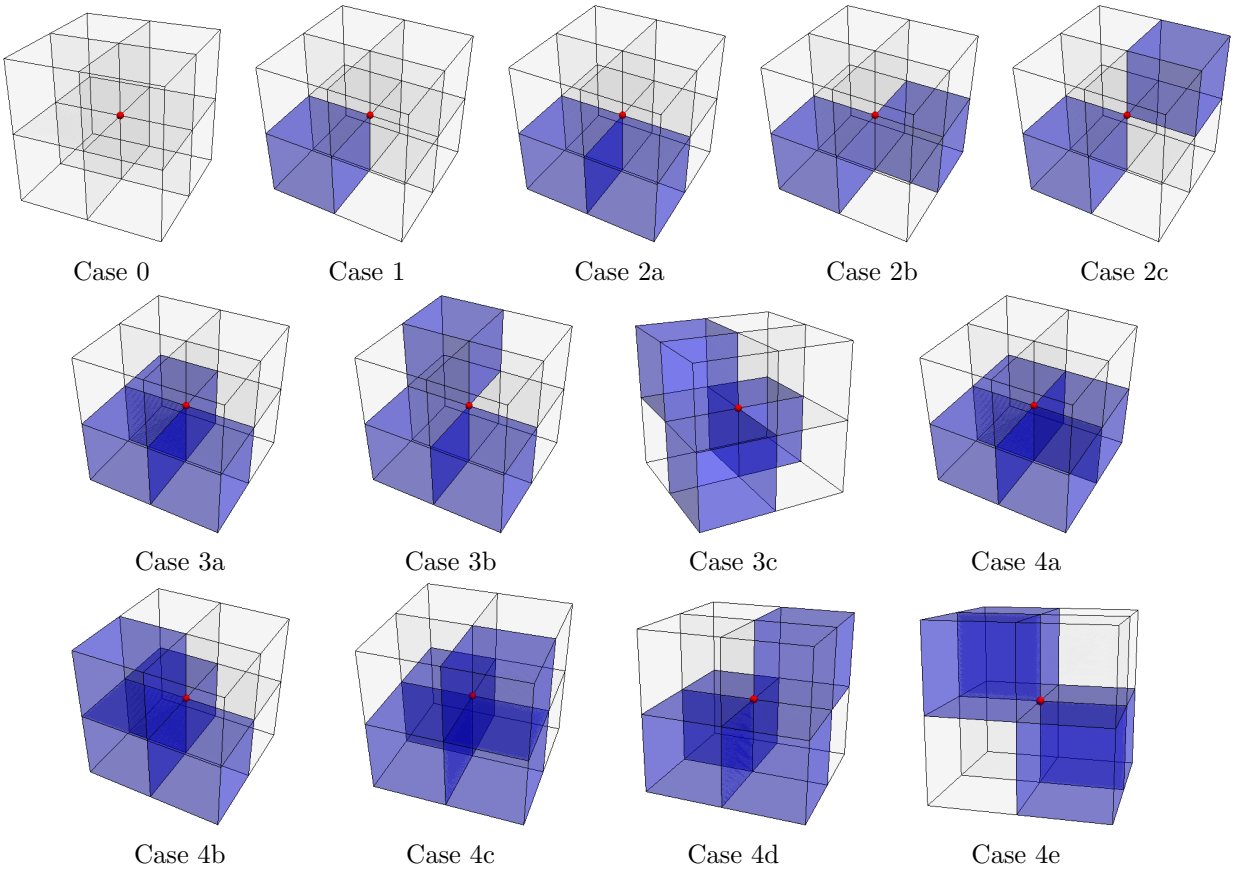


Figure 19: Possible cases in 3D where linear dependence may occur. The vertex-associated function of interest is associated with the red circle, and irregular elements are shaded blue. Cases involving more than four irregular elements can still be shown using these figures, where irregular and regular elements are shaded white and blue, respectively.

and $C^1$ B-splines, respectively, with certain $C^2$ B-splines truncated with respect to $C^1$ B-splines. Linear dependence occurs only when a (truncated) vertex-associated function $B^v_{t,i}$ can be represented by a linear combination of other (truncated) vertex-associated functions $B^v_{t,j}$ and active face-point-associated functions $B^f_{a,k}$. Under the assumption of linear dependence, we have

$$B^v_{t,i} = \sum_j c_{ij} B^v_{t,j} + \sum_k d_{ik} B^f_{a,k}, \tag{44}$$

where $c_{ij}$ and $d_{ik}$ are the corresponding coefficients.

Recall that a vertex-associated function can be expressed in term of its face-point-associated children (here only $C^1$ B-splines), where we only need to study its one-ring neighborhood. Because of the local linear independence of classical B-splines, a necessary condition for Eq. (44) to hold is that, on the regular subdomain, the face-point-associated children of $B^v_{t,i}$ coincide with $B^f_{a,k}$ and the face-point-associated children of $B^v_{t,j}$. We actually do not need to include $B^f_{a,k}$ since all $d_{ik}$ must be zero according to the truncation mechanism. Next we only consider $B^v_{t,i}$ and $B^v_{t,j}$ and we represent them using their face-point-associated children in matrix form $\mathbf{B}^v_t = \mathbf{M}\mathbf{B}^f$, where all the face-point-associated children $\mathbf{B}^f$ are $C^1$ B-splines and they are linearly independent, and $\mathbf{M}$ can be obtained by assembling matrices in Eqs. (3) and (15). We then only need to check the rank of $\mathbf{M}$. Depending on the configurations of irregular elements (shaded blue) in the one-ring neighborhood of $B^v_{t,i}$, we have five cases in 2D (Fig. 18) and thirteen cases in 3D (Fig. 19) where linear dependence may occur. In Fig. 18, $B^v_{t,i}$, $B^v_{t,j}$ and their face-point-associated children are marked with red open squares, black open squares and green open circles, respectively. In Fig. 19, $B^v_{t,i}$ is marked with red circles and $B^v_{t,j}$ are associated with all the corners of white elements. It is easy to verify that $\mathbf{M}$ has full rank for all the cases in both 2D and 3D. Therefore, $B^v_{t,i}$ and $B^v_{t,j}$ are linearly independent, which contradicts the assumption in Eq. (44). This concludes that (truncated) vertex-associated functions and face-point-associated functions are linearly independent on the regular subdomain.

Then we only need to verify linear independence of the spline functions with support fully contained in the irregular subdomain, which are face-point-associated functions and Bézier functions. Actually, linear independence of these functions has been proved in Proposition 4.2 in [26]. This concludes the proof.

□

## 6. Numerical Examples and Discussions

In this section, we apply the blended B-spline construction to two quad meshes in Fig. 20 and three hex meshes in Figs. 21−23 and verify that the blended construction yields optimal convergence rates. We summarize the statistics of these five input meshes in Table 4.

Table 4: Statistics of input control meshes

| Models | # Vertices | # Elements | # Extraordinary points (interior) | # Irregular elements (interior) |
|---|---|---|---|---|
| Square | 143 | 120 | 8 | 13 |
| Manifold | 161 | 128 | 23 | 99 |
| Cube | 517 | 448 | 24 | 56 |
| Rod | 2,011 | 1,376 | 24 | 56 |
| Hook | 6,327 | 5,121 | 2,572 | 3,952 |

We first test the $C012$ construction by solving Poisson's equation on planar unstructured quad meshes. Two input control meshes are studied: one discretizing a square domain and the other defining a manifold domain; see Fig. 20(a, d), respectively. We adopt the same exact solution for both meshes,

$$u(x, y) = xy(1 - x)(1 - y)(1 + y\sin(x) + x\sin(y)). \tag{45}$$

For each model, Dirichlet boundary conditions are imposed on the entire boundary. The boundary conditions can be strongly or weakly imposed. Since only Bézier functions are defined on the boundary and they are non-interpolatory, we perform a least-square fitting for a strong imposition to approximate the given Dirichlet data. Nitsche's method is adopted for a weak imposition [11]. We observe that strong imposition and weak imposition yield almost the same results (i.e., the $L^2$ and $H^1$ error). We create a series of meshes through global refinement, and build blended spline functions on each of them. In Fig. 20(b, e), we plot the convergence curves of the $L^2$- and $H^1$-norm errors with respect to the maximum element size ($h_{\max}$). We observe optimal convergence rates for both models. Note that when bicubic splines are used as a basis, the optimal convergence rate is 4.0 for the $L^2$-norm error and 3.0 for the $H^1$-norm error. Plotting convergence curves in terms of the square root of DOF in Fig. 20(c, f) shows optimal rates as well.

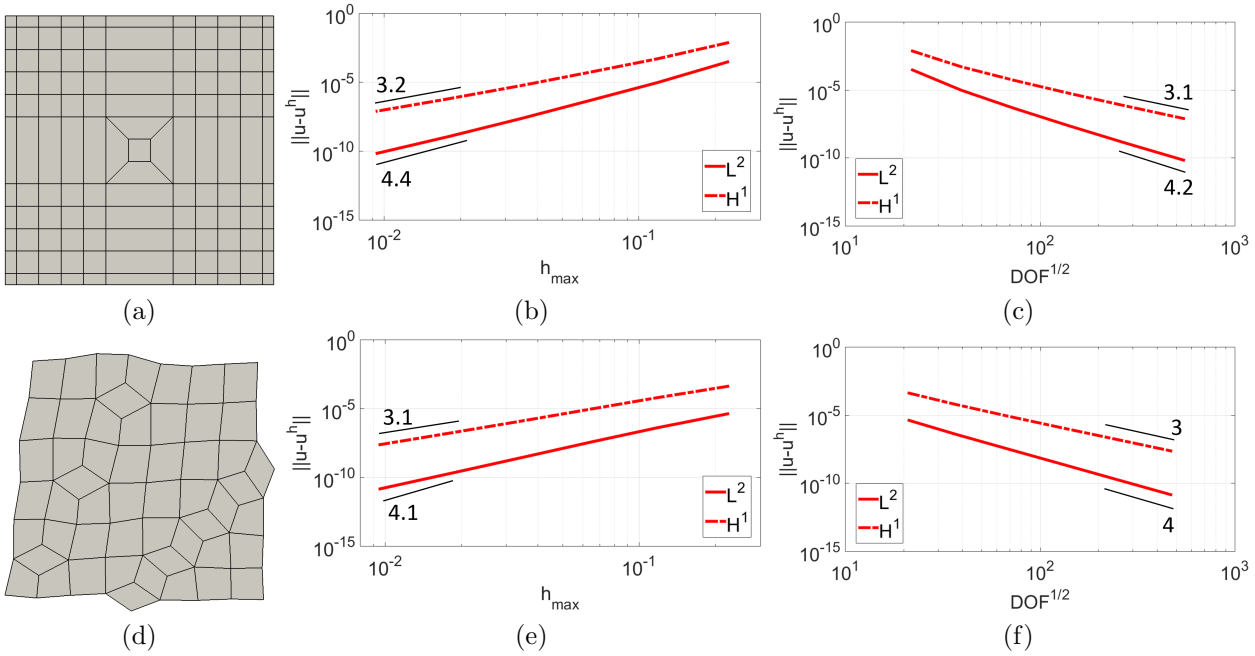


Figure 20: Solving Poisson's equation on a square domain (a−c) and on a manifold domain (d−f). (a, d) Input control meshes, (b, e) convergence curves with respect to the maximum element size ($h_{\max}$), and (c, f) convergence curves with respect to the square root of DOF ($\mathrm{DOF}^{1/2}$).

Next for 3D models, we first perform a patch test by solving Poisson's equation on a unit cube domain $[0,1]^3$. The input control mesh is shown in Fig. 21(a), where general 3D extraordinary vertices (not generated by sweeping 2D ones) are allowed; see the red circle for example. The solution field is given as $u(x,y,z) = x$. Dirichlet boundary conditions are strongly imposed at boundary faces $x = 0$ and $x = 1$. We solve the problem using three blended constructions: $C012$, $C02$ and $C02i$ constructions. Recall that $C02$ and $C02i$ constructions are identical on an input mesh. The patch test is passed with machine precision under all three constructions, with the overall $L^2$ and $H^1$ errors in the order of $10^{-15}$ and $10^{-14}$, respectively. Similar results are observed for patch tests along $y$ and $z$ directions.

We further study the convergence behavior on three 3D models; see their corresponding input control meshes in Figs. 21(a), 22(a) and 23(a). Poisson's equation is still adopted with the following two exact solutions,

$$u(x,y,z) = \sin(\pi x)\sin(\pi y)\sin(\pi z) \tag{46}$$

and

$$u(x,y,z) = e^{(x+y+z)/3}. \tag{47}$$

As in 2D, only Dirichlet boundary conditions are considered. They can be strongly or weakly imposed, yielding almost the same results ($L^2$ and $H^1$ error) in our tests. For each model, we apply all three

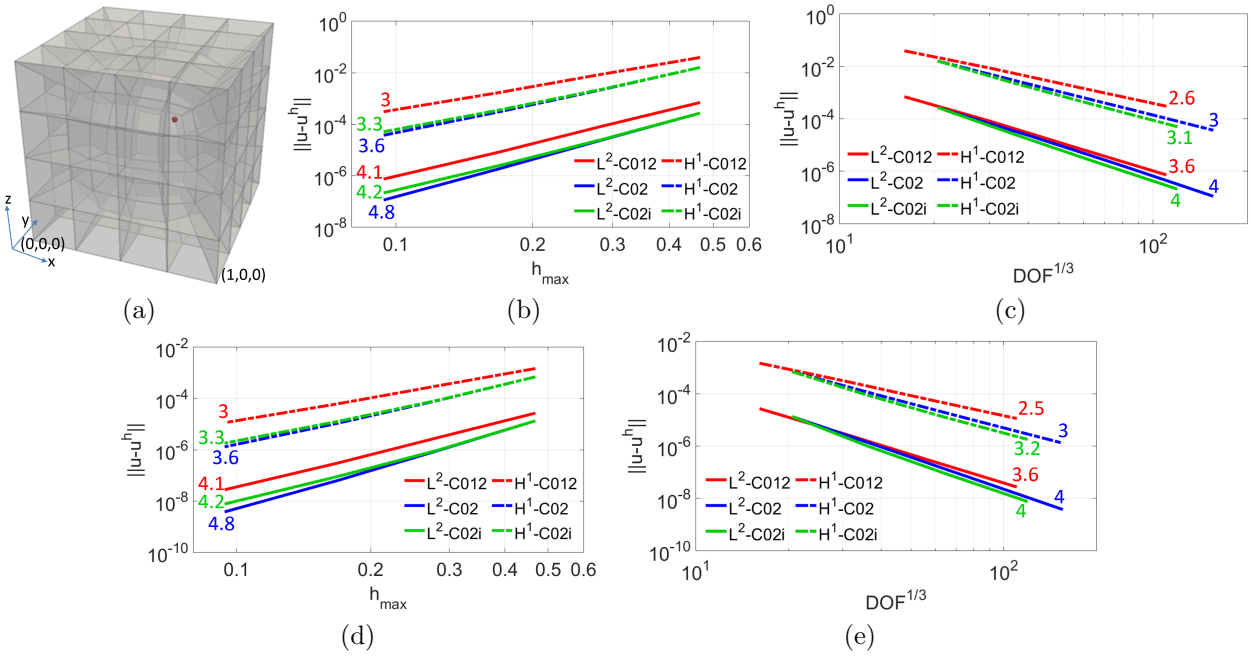


Figure 21: Solving Poisson's equation on a cube model. (a) The input control mesh, (b, c) convergence to the exact solution in Eq. (46), and (d, e) convergence to the exact solution in Eq. (47).

constructions ($C012$, $C02$ and $C02i$). Global refinement is performed for each model. All the computations of the 3D models were carried out in the Bridges system at the Pittsburgh Supercomputing Center [28, 18]. In Figs. 21−23, the convergence curves are plotted with respect to the maximum element size ($h_{\max}$) as well as the cube root of DOF (DOF$^{1/3}$). The $L^2$-norm error is shown in solid lines whereas the $H^1$-norm error is shown in dashed lines. Red, blue and green curves are results using $C012$, $C02$ and $C02i$ constructions, respectively. We can observe even faster convergence rates than the optimal ones when the rates are plotted with respect to $h_{\max}$. We also observe that given the same element size, $C02$ and $C02i$ constructions introduce more DOF and thus yield smaller error compared to the $C012$ construction.

When plotting them with respect to DOF$^{1/3}$, the convergence rates are slightly different from those computed in terms of $h_{\max}$. This is because the change of DOF$^{1/3}$ is not the same as the change of $h_{\max}$ during refinement. We define a ratio to measure these changes

$$\gamma = \log\left(\frac{\text{DOF}^{1/3} \text{ of refined mesh}}{\text{DOF}^{1/3} \text{ of given mesh}}\right) / \log\left(\frac{h_{\max} \text{ of given mesh}}{h_{\max} \text{ of refined mesh}}\right). \tag{48}$$

For each 3D model, the ratio $\gamma$ is constant for a specific blended construction; see Table 5. We can observe that $\gamma$ is always larger than 1.0, which is caused by introducing extra DOF in the blended constructions. In addition, $\gamma$ is particularly large in the hook model, where there is a large portion of irregular elements with many extra DOF introduced. Note that in the rod model shown in Fig. 22, all the extraordinary vertices can be obtained by sweeping 2D counterparts and optimal convergence rates are achieved with respect to both $h_{\max}$ and DOF$^{1/3}$.

We define another ratio called the *DOF/element ratio* as the total DOF divided by the number of elements. In Table 6, we summarize this ratio for each hex model in three blended constructions. Compared to the cube and rod models, the hook model contains the most extraordinary vertices where many extra DOF are introduced in irregular elements. Therefore, its DOF/element ratio is also the largest. In each construction, the DOF/element ratio decreases as global refinement proceeds, and the change of the ratio between two consecutive refinement steps becomes smaller and smaller. As expected, a $C02$ blended construction generally needs a lot more DOF than a $C012$ construction. We also observe that even though

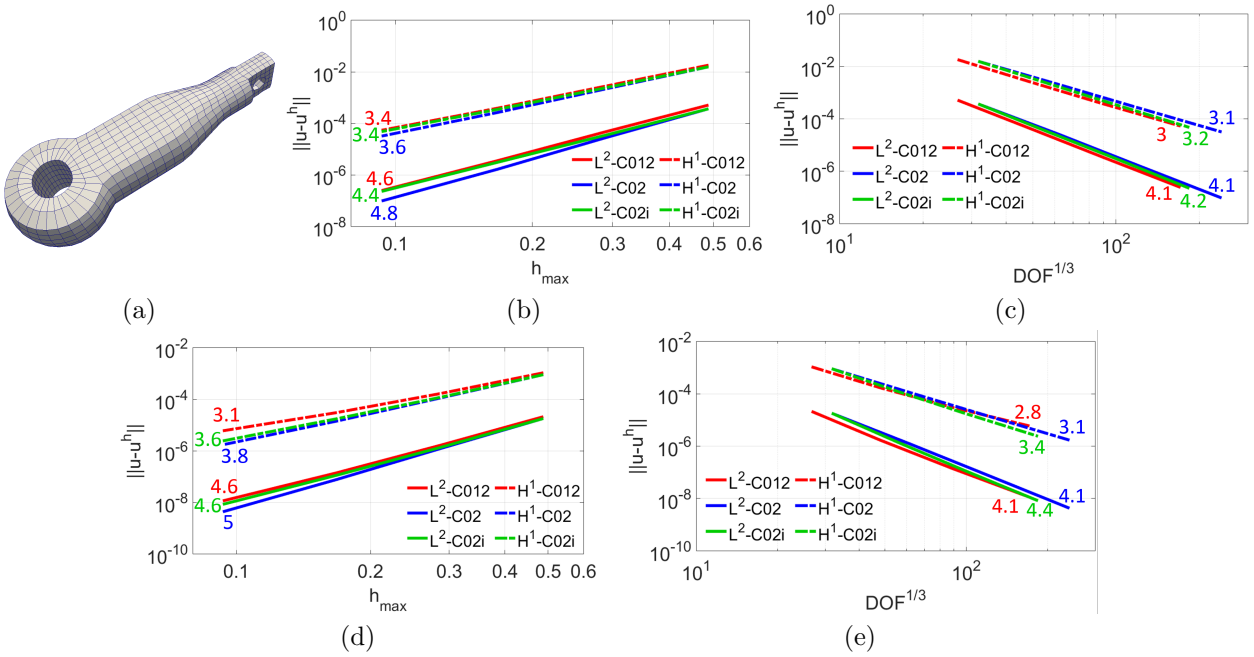


Figure 22: Solving Poisson's equation on a rod model. (a) The input control mesh, (b, c) convergence to the exact solution in Eq. (46), and (d, e) convergence to the exact solution in Eq. (47).

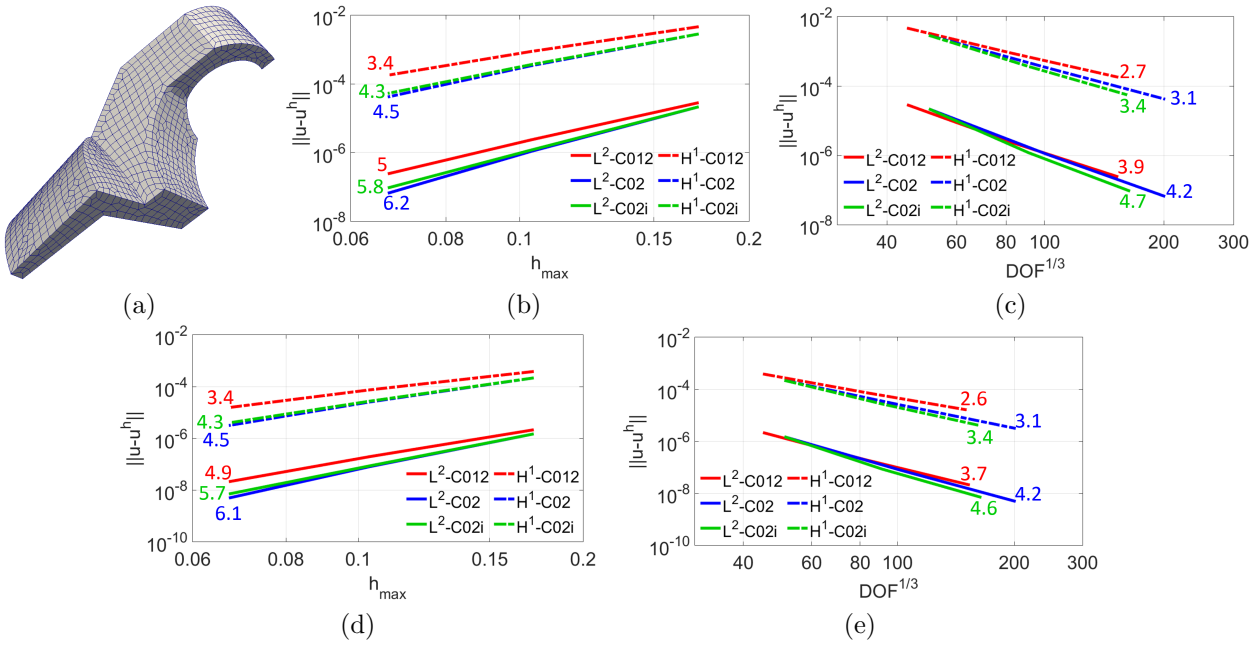


Figure 23: Solving Poisson's equation on a hook model. (a) The input control mesh, (b, c) convergence to the exact solution in Eq. (46), and (d, e) convergence to the exact solution in Eq. (47).

Table 5: The ratio $\gamma$ in unstructured hex meshes

| Models | $C012$ construction | $C02$ construction | $C02i$ construction |
|---|---|---|---|
| Cube | 1.18 | 1.2 | 1.06 |
| Rod | 1.12 | 1.2 | 1.06 |
| Hook | 1.32 | 1.46 | 1.23 |

$C02$ and $C02i$ constructions have the same DOF/element ratio in the input mesh, the ratio decreases much faster in a $C02i$ construction because it introduces many fewer DOF in each refinement step. Moreover, the DOF/element ratio becomes large even in a $C012$ construction if an input hex mesh is unstructured with many extraordinary vertices (e.g. the hook model), where many Bézier points are introduced in irregular elements.

Table 6: The DOF/element ratio during refinement

| | $C012$ construction | | | | $C02$ construction | | | | $C02i$ construction | | | |
|---|---|---|---|---|---|---|---|---|---|---|---|---|
| Refinement step | 0 | 1 | 2 | 3 | 0 | 1 | 2 | 3 | 0 | 1 | 2 | 3 |
| Cube | 9.6 | 7.7 | 6.4 | 5.7 | 20.0 | 17.6 | 16.5 | 16.0 | 20.0 | 13.4 | 9.4 | 7.2 |
| Rod | 14.3 | 10.2 | 8.0 | 6.9 | 24.0 | 21.2 | 20.0 | 19.2 | 24.0 | 16.1 | 11.3 | 8.6 |
| Hook | 18.2 | 13.8 | 10.8 | N/A | 26.6 | 25.1 | 24.4 | N/A | 26.6 | 18.5 | 13.2 | N/A |

In summary, all the three blended constructions can yield optimal convergence rates with respect to the maximum element size. $C02$ and $C02i$ constructions generally exhibit slightly higher convergence rates than the $C012$ construction, so they are better options when only global refinement is needed. However, they introduce many more DOF to the input mesh than the $C012$ construction; see the DOF/element ratio at refinement step 0 in Table 6. When local refinement is desired, the $C012$ construction serves as the most efficient candidate, because it introduces the minimal extra DOF and minimum $C^0$ faces/edges/vertices to the input mesh. We will further study local refinement based on the blended B-spline construction in the future.

## 7. Conclusion and Future Work

In this paper, we have presented a new blended B-spline method exhibiting optimal convergence rates when unstructured quad/hex meshes are taken as control meshes in IGA. Various spline functions are defined on different types of elements, with the truncation mechanism employed to connect regular and irregular patches. Three blended constructions ($C012$, $C02$ and $C02i$) were studied, each introducing a different number of DOF and possessing different properties (Table 3). In all these blended constructions, spline functions form a non-negative partition of unity, are linearly independent, and preserve consistent parameterization in refinement. We investigated these three blended constructions in IGA and observed optimal convergence rates in all the tested 2D and 3D models.

In the future, applying the blended B-spline construction to the Kirchhoff-Love shell would be promising [6], where we need to impose $G^1$ continuity around 2D extraordinary vertices instead of $C^0$. Building hierarchical splines based on a blended B-spline construction would also be interesting, where we can rigorously study local refinement on unstructured hex meshes. Another problem worthy of investigation is the memory-efficient storage of Bézier extraction matrices in 3D. When tricubic splines are used, the dimension of such matrices for each element is in the order of $64 \times 64$. Currently such matrices are stored as dense matrices in our implementation. Switching to sparse matrices could significantly reduce memory consumption. Another challenging problem is how to impose $G^1$ continuity across spoke faces in an unstructured hex mesh. This problem has not been studied in the literature.

**Acknowledgements**

X. Wei and Y. Zhang were supported in part by the PECASE Award N00014-16-1-2254 and NSF CAREER Award OCI-1149591. D. Toshniwal and T.J.R. Hughes were partially supported by the Office of Naval Research (Grant Nos. N00014-17-1-2119, N00014-17-1-2039, and N00014-13-1-0500), and by the Army Research Office (Grant No. W911NF-13-1-0220). H. Speleers and C. Manni were supported by the MIUR Futuro in Ricerca 2013 Programme through the project DREAMS (RBFR13FBI3). X. Li was supported by the NKBRPC (2011CB302400), SRF for ROCS SE, and the Youth Innovation Promotion Association CAS. J. A. Evans was supported by the Air Force Office of Scientific Research under Grant No. FA9550-14-1-0113. This work used the Extreme Science and Engineering Discovery Environment (XSEDE), which is supported by National Science Foundation grant number OCI-1053575. In particular, we run our codes on the Bridges system (NSF award number ACI-1445606) at the Pittsburgh Supercomputing Center (PSC).

## Appendix A: Alternative Blended B-Spline Constructions

In addition to the $C012$ blended construction in Sections 3 and 4, we here present two alternatives. One is the $C02$ construction, which only involves vertex-associated functions $B_i^v$ and Bézier functions $B_k^0$. The other, called the $C02i$ construction, is an improvement of $C02$ by introducing fewer DOF in refinement.

Compared to the $C012$ construction, the $C02$ construction utilizes different ways to address: (1) how $C^0$ tags are assigned in Step 1, and (2) how $C^0$ tags pass on in refinement. Recall that in a $C012$ construction, $C^0$ tags are assigned to extraordinary edges/vertices, spoke faces/edges and boundary faces/edges/vertices. In contrast, the $C02$ construction assigns $C^0$ tags to all the faces, edges and vertices of an irregular element; see Fig. 24(a, b) for a comparison, where the red open square and red edges represent a $C^0$ vertex and $C^0$ edges, respectively. As a result, more Bézier points are introduced in the $C02$ construction and all face-point-associated functions $B_j^f$ (or body-point-associated functions $B_j^b$) are essentially Bézier functions $B_k^0$ after truncation. Therefore, only $B_k^0$ have influence on each irregular element. In other words, the Bézier representation is employed for each irregular element. On the other hand, only uniform $C^2$ B-splines are defined on a regular non-transition element, whereas both $B_i^v$ and $B_k^0$ are defined on a regular transition element. Given an irregular element (shaded blue) in Fig. 24(b), all its edges and vertices are assigned with $C^0$ tags in the $C02$ construction, so all the corresponding 16 $B_k^0$ (red circles) are added. Some of these $B_k^0$ also have support on neighboring regular transition elements. As shown in Fig. 24(c, d), a regular transition element (shaded orange) may share either an edge (Case 1) or only a vertex (Case 2) with this irregular element, where those $B_k^0$ associated with red circles have support on the orange element. In Table 7, we summarize the types of spline functions ($B_i^v$, $B_j^f$ and $B_k^0$) defined on different elements for the $C02$ and $C02i$ constructions in 2D.

Table 7: Possible spline functions defined on different types of elements in $C02$ and $C02i$ constructions

| Construction type | $C02$ construction | | | $C02i$ construction | | |
|---|---|---|---|---|---|---|
| Element type | $B_i^v$ | $B_j^f$ | $B_k^0$ | $B_i^v$ | $B_j^f$ | $B_k^0$ |
| Regular non-transition | Yes | No | No | Yes | No | No |
| Irregular non-transition | No | No | Yes | No | Yes | Yes |
| Regular transition | Yes | No | Yes | Yes | No | Yes |
| Irregular transition | No | No | Yes | No | Yes | Yes |

Truncation is only needed in regular transition elements, where certain $B_i^v$ are truncated with respect to active Bézier children. Compared with Fig. 5(b, c), after truncation of involved $B_i^v$ in Fig. 24(c, d), the ordinates of the functions associated with black open squares are all zero on the orange element. In other words, these truncated $B_i^v$ do not have support on it. Therefore, only the remaining truncated $B_i^v$ (black filled squares) and added $B_k^0$ (red circles[4]) are defined on a regular transition element, and the total number

[4]Note that two red circles overlay with black filled squares in Fig. 24(c) and one red circle overlays with a black filled square in Fig. 24(d).

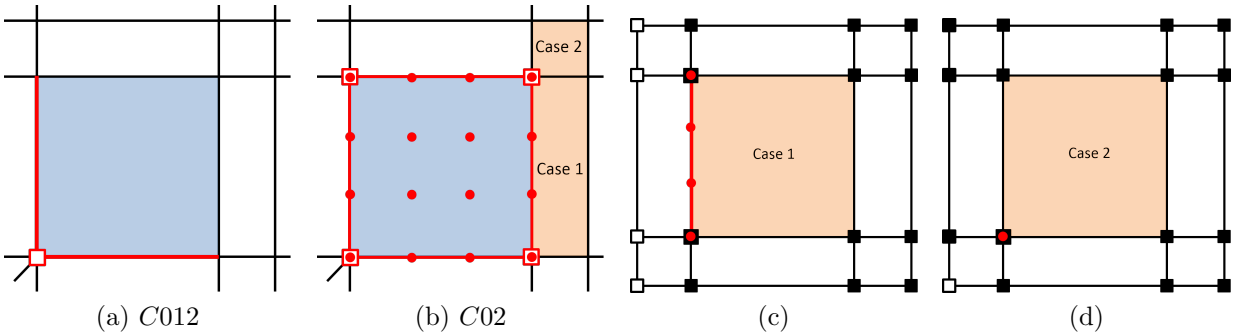


Figure 24: (a) $C^0$ edges (red edges) and a $C^0$ vertex (the red open square) in the $C012$ construction, (b) $C^0$ edges (red edges) and $C^0$ vertices (red open squares) in the $C02$ construction, and (c, d) two cases of Bézier functions $B_k^0$ with support on a regular transition element (shaded orange). In (a, b), the blue shade is an irregular element and red circles represent added $B_k^0$. In (c, d), the black filled squares and black open squares represent truncated vertex-associated functions $B_i^v$ with and without support on the orange element, respectively.

of these functions is always 16. Moreover, it is easy to verify that these 16 functions are locally linearly independent on the regular transition element (shaded orange) since the underlying Bézier extraction matrix (with truncation) is a $16 \times 16$ matrix of full rank. The same argument can be easily extended to 3D, where a regular transition element may share a face, an edge or a vertex with a neighboring irregular element. We show these three cases in Fig. 25, where the regular transition element and its neighboring irregular element are shaded orange and blue, respectively. Red circles represent added $B_k^0$ to the orange element, whereas black circles represent $B_i^v$ that no longer have support on the orange element after truncation. In all cases, there are always 64 functions defined on a regular transition element. Furthermore, it can be verified that the Bézier extraction matrix (with truncation) in each case is a $64 \times 64$ matrix of full rank.

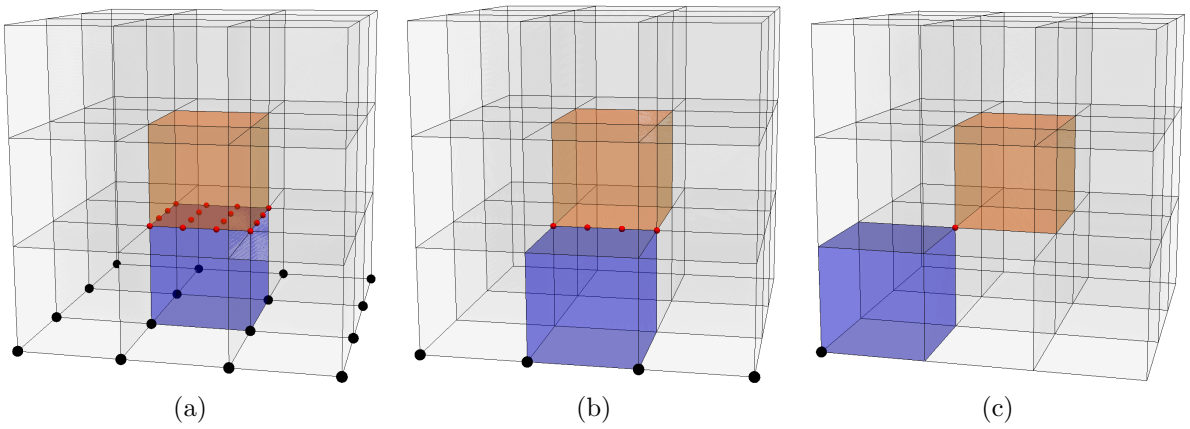


Figure 25: A regular transition element (shaded orange) sharing a face (a), an edge (b) or a vertex (c) with a neighboring irregular element (shaded blue). Red circles represent added Bézier functions $B_k^0$ to the orange element, whereas black circles represent vertex-associated functions $B_i^v$ that no longer have support on the orange element after truncation.

Refinement in the $C02$ construction is the same as that of the $C012$ construction, except the step of how to update $C^0$ tags in the refined mesh. In the $C02$ construction, all the sub-elements of an irregular element are irregular and all the newly generated faces/edges/vertices involving refinement of an irregular element are assigned with $C^0$ tags. As a result, the Bézier representation is also used for all the sub-elements of an irregular element; see Fig. 13(b). Passing $C^0$ tags in such a "dense" manner is easy for implementation, where every patch is determined by either a Bézier control mesh or a uniform B-spline control mesh.

We then introduce the $C02i$ construction, an improved version of the $C02$ construction that introduces fewer DOF during refinement. During refinement, instead of assigning all the newly generated

faces/edges/vertices of an irregular element with $C^0$ tags, we follow the same way as in the $C012$ construction to assign $C^0$ tags to: (1) sub-faces, newly generated edges and the center vertex of each $C^0$ face, (2) sub-edges and the midpoint of each $C^0$ edges, and (3) existing $C^0$ vertices. As a result, the $C02i$ construction introduces $B_j^f$ or $B_j^b$ within the irregular submesh, while leaving $B_k^0$ on the interface of irregular and regular submeshes. Fig. 13(c) shows an example of the $C02i$ construction on the refined mesh of Fig. 24(a). $C^0$ edges are marked in red, whereas $B_j^f$ and $B_k^0$ are represented by green circles and red circles, respectively. The types of functions defined on different elements are also summarized in Table 7. Performing truncation in a regular transition element is the same as the $C02$ construction, while truncating $B_j^f$ with respect to active Bézier children is the same as in the $C012$ construction. Local linear independence can be verified in the similar manner as in the $C02$ construction.

It can be shown that both $C02$ and $C02i$ constructions give rise to locally linearly independent spline functions. This is an advantage over the $C012$ construction, which only features (global) linear independence. Compared with the C012 construction, the implementation of $C02$ and $C02i$ constructions is easier because they have at most two types of functions defined on a particular element, whereas all three types of functions are involved in the $C012$ construction (e.g., on an irregular transition element). On the other hand, $C02$ and $C02i$ constructions require more DOF as illustrated in the testing examples in Section 6.

## References


[1] W. Boehm. Inserting new knots into B-spline curves. *Computer-Aided Design*, 12(4):199–201, 1980.

[2] W. Boehm and A. Müller. On de Casteljau's algorithm. *Computer Aided Geometric Design*, 16(7):587 – 605, 1999.

[3] P. B. Bornermann and F. Cirak. A subdivision-based implementation of the hierarchical B-spline finite element method. *Computer Methods in Applied Mechanics and Engineering*, 253:584–598, 2013.

[4] F. Buchegger, B. Jüttler, and A. Mantzaflaris. Adaptively refined multi-patch B-splines with enhanced smoothness. *Applied Mathematics and Computation*, 272:159–172, 2016.

[5] D. Burkhart, B. Hamann, and G. Umlauf. Iso-geometric finite element analysis based on Catmull-Clark subdivision solids. *Computer Graphics Forum*, 29:1575–1584, 2010.

[6] H. Casquero, L. Liu, Y. Zhang, A. Reali, J. Kiendl, and H. Gomez. Arbitrary-degree T-splines for isogeometric analysis of fully nonlinear Kirchhoff-Love shells. *Computer-Aided Design*, 82:140–153, 2017.

[7] A. Collin, G. Sangalli, and T. Takacs. Approximation properties of multi-patch $C^1$ isogeometric spaces. 2015. arXiv preprint arXiv:1509.07619.

[8] J. A. Cottrell, T. J. R. Hughes, and Y. Bazilevs. Isogemetric analysis: toward integration of CAD and FEA. John Wiley & Sons, 2009.

[9] C. de Boor. *A Practical Guide to Splines*. Springer, 2001. Revised edition.

[10] J. Deng, F. Chen, X. Li, C. Hu, W. Tong, Z. Yang, and Y. Feng. Polynomial splines over hierarchical T-meshes. *Graphical Models*, 70:76–86, 2008.

[11] A. Embar, J. Dolbow, and I. Harari. Imposing Dirichlet boundary conditions with Nitsche's method and spline-based finite elements. *International Journal for Numerical Methods in Engineering*, 83(7):877–898, 2010.

[12] C. Giannelli, B. Jüttler, and H. Speleers. THB-splines: the truncated basis for hierarchical splines. *Computer Aided Geometric Design*, 29:485–498, 2012.

[13] T. J. R. Hughes, J. A. Cottrell, and Y. Bazilevs. Isogeometric analysis: CAD, finite elements, NURBS, exact geometry and mesh refinement. *Computer Methods in Applied Mechanics and Engineering*, 194:4135–4195, 2005.

[14] M. Kapl, V. Vitrih, B. Jüttler, and K. Birner. Isogeometric analysis with geometrically continuous functions on two-patch geometries. *Computers and Mathematics with Applications*, 70(7):1518–1538, 2015.

[15] M. Majeed and F. Cirak. Isogeometric analysis using manifold-based smooth basis functions. *Computer Methods in Applied Mechanics and Engineering*, 316:547–567, 2017.

[16] T. Nguyen, K. Karčiauskas, and J. Peters. A comparative study of several classical, discrete differential and isogeometric methods for solving Poisson's equation on the disk. *Axioms*, 3:280–300, 2014.

[17] T. Nguyen and J. Peters. Refinable $C^1$ spline elements for irregular quad layout. *Computer Aided Geometric Design*, 43:123–130, 2016.

[18] N. A. Nystrom, M. J. Levine, R. Z. Roskies, and J. R. Scott. Bridges: a uniquely flexible HPC resource for new communities and data analytics. In *Proceedings of the 2015 XSEDE Conference: Scientific Advancements Enabled by Enhanced Cyberinfrastructure*, pages 30:1–30:8, 2015.

[19] L. Piegl and W. Tiller. *The NURBS Book (2nd Ed.)*. Springer-Verlag New York, Inc., 1997.

[20] U. Reif. A refineable space of smooth spline surfaces of arbitrary topological genus. *Journal of Approximation Theory*, 90(2):174–199, 1997.

[21] M. A. Scott. *T-splines as a Design-Through-Analysis Technology*. PhD thesis, The University of Texas at Austin, 2011.

[22] M. A. Scott, X. Li, T. W. Sederberg, and T. J. R. Hughes. Local refinement of analysis-suitable T-splines. *Computer Methods in Applied Mechanics and Engineering*, 213-216:206–222, 2012.

[23] M. A. Scott, R. N. Simpson, J. A. Evans, S. Lipton, S. P. A. Bordas, T. J. R. Hughes, and T. W. Sederberg. Isogeometric boundary element analysis using unstructured T-splines. *Computer Methods in Applied Mechanics and Engineering*, 254:197–221, 2013.

[24] M. A. Scott, D. C. Thomas, and E. J. Evans. Isogeometric spline forests. *Computer Methods in Applied Mechanics and Engineering*, 269(0):222–264, 2014.

[25] T. W. Sederberg, J. Zheng, A. Bakenov, and A. Nasri. T-splines and T-NURCCs. *ACM Transactions on Graphics*, 22:477–484, 2003.

[26] D. Toshniwal, H. Speleers, and T. J. R. Hughes. Analysis-suitable spline spaces of arbitrary degree on unstructured quadrilateral meshes. 2017. ICES REPORT 17-16, Institute for Computational Engineering and Sciences, The University of Texas at Austin.

[27] D. Toshniwal, H. Speleers, and T. J. R. Hughes. Smooth cubic spline spaces on unstructured quadrilateral meshes with particular emphasis on extraordinary points: geometric design and isogeometric analysis considerations. *Computer Methods in Applied Mechanics and Engineering*, 2017. DOI: 10.1016/j.cma.2017.06.008.

[28] J. Towns, T. Cockerill, M. Dahan, I. Foster, K. Gaither, A. Grimshaw, V. Hazlewood, S. Lathrop, D. Lifka, G. D. Peterson, R. Roskies, J. R. Scott, and N. Wilkins-Diehr. XSEDE: accelerating scientific discovery. *Computing in Science & Engineering*, 16(5):62–74, 2014.

[29] W. Wang, Y. Zhang, L. Liu, and T. J. R. Hughes. Trivariate solid T-spline construction from boundary triangulations with arbitrary genus topology. *A Special Issue of Solid and Physical Modeling 2012 in Computer Aided Design*, 45:351–360, 2013.

[30] W. Wang, Y. Zhang, G. Xu, and T. J. R. Hughes. Converting an unstructured quadrilateral/hexahedral mesh to a rational T-spline. *Computational Mechanics*, 50:65–84, 2012.

[31] X. Wei, Y. Zhang, and T. J. R. Hughes. Truncated hierarchical tricubic $C^0$ spline construction on unstructured hexahedral meshes for isogeometric analysis applications. *Computers and Mathematics with Applications*, 74(9):2203–2220, 2017.

[32] X. Wei, Y. Zhang, T. J. R. Hughes, and M. A. Scott. Truncated hierarchical Catmull-Clark subdivision with local refinement. *Computer Methods in Applied Mechanics and Engineering*, 291:1–20, 2015.

[33] X. Wei, Y. Zhang, T. J. R. Hughes, and M. A. Scott. Extended truncated hierarchical Catmull-Clark subdivision. *Computer Methods in Applied Mechanics and Engineering*, 299:316–336, 2016.

[34] X. Wei, Y. Zhang, L. Liu, and T. J. R. Hughes. Truncated T-splines: fundamentals and methods. *Computer Methods in Applied Mechanics and Engineering*, 316:349–372, 2017.

[35] X. Yuan and K. Tang. Rectified unstructured T-splines with dynamic weighted refinement for improvement in geometric consistency and approximation convergence. *Computer Methods in Applied Mechanics and Engineering*, 316:373–399, 2017. Special Issue on Isogeometric Analysis: Progress and Challenges.

[36] Y. Zhang. *Geometric Modeling and Mesh Generation from Scanned Images*. Chapman and Hall/CRC, 2016.